REPRODUCED AT GOV'T EXPENSE # 5

KAPL-P-000125
(K98169)

HIGH PRESSURE ANNULAR TWO-PHASE FLOW IN A NARROW DUCT

CONF-990702--

T. A. Trabold, R. Kumar

July 1999

DISTRIBUTION OF THIS DOCUMENT IS UNLIMITED

MASTER

NOTICE

KAPL ATOMIC POWER LABORATORY SCHENECTADY, NEW YORK 12501

Operated for the U. S. Department of Energy
by KAPL, Inc. a Lockheed Martin company

High Pressure Annular Two-Phase Flow in a Narrow Duct. Part I: Local Measurements in the Droplet Field

Thomas A. Trabold and Ranganathan Kumar
Lockheed Martin Corporation
Schenectady, NY 12301

ABSTRACT

Detailed measurements have been made in a high pressure, adiabatic (boiled at the inlet) annular flow in a narrow, high aspect ratio duct using a gamma densitometer, hot-film anemometer and high-speed video photography. Measurements of void fraction, droplet frequency, velocity, drop size, and interfacial area concentration have been made to support the three-field computational capability. An important aspect of this testing is the use of a modeling fluid (R-134a) in a vertical duct which permits visual access in annular flow. This modeling fluid accurately simulates the low liquid-to-vapor density ratio of steam-water flows at high pressures.

These measurements have been taken in a narrow duct of hydraulic diameter 4.85 mm, and a cross-section aspect ratio of 22.5. However, the flow displays profiles of various shapes not only in the narrow dimension, but also in the width dimension. In particular, the shape of the droplet profiles depends on the entrained droplet flux from the edges in the vapor core. The average diameter from these profiles compare well with the models developed in the literature. Interfacial area concentration for these low density ratio flows is higher than the highest concentration reported for air-water flows. Video records show that along with the bow-shaped waves, three-dimensional λ-shaped waves appear in annular flows for high flow rates.

Nomenclature

a_i	Interfacial area concentration
B	Measurement bias
D_h	Duct hydraulic diameter
d_m	Volume mean droplet diameter
d_{sm}	Sauter mean droplet diameter
f_d	Droplet frequency
G	Mass flux
j	Superficial velocity
L	Test section length
P	Pressure
Re	Reynolds number
$S_{\bar{x}}$	Precision index
t	Duct thickness
t_{95}	Student's t for 95% confidence
u	Mean phasic velocity
U	Measurement uncertainty
V	HFA output voltage
V_d	Droplet velocity
W	Duct width
We_m	Modified Weber number
w	Mass flow rate
x	Quality
X	Streamwise (length) dimension
Y	Transverse (width) dimension
Z	Spacing (thickness) dimension

Greek Symbols

α, $\bar{\alpha}$	Void fraction
$\Delta\rho$	Density difference
μ	Dynamic viscosity
ρ	Density
σ	Surface tension
τ_m	Time associated with maximum cross-correlation factor

Subscripts

d	Droplet field
g	Gas phase
l	Liquid phase
w	Wave

Introduction

The inception of wall-heated two-phase annular flow occurs through a complex flow regime transition. The annular flow regime consists of a liquid film on the wall and a vapor core with droplets formed from the shearing of the roll waves. Hewitt and Hall-Taylor (1970) discussed the physical mechanisms that occur in annular flow and the physical models that describe these mechanisms. In order to delineate the heat transfer effects, researchers have performed adiabatic tests in two immiscible fluids such as air and water. In fact, most of the correlations and models in annular flow such as interfacial shear, entrainment/deposition and droplet motion have been validated using air-water experiments. However, to date, the integrated effects of these physical mechanisms in annular flow have not been captured and compared with local measurements of void fraction and droplet velocity.

While the flow pattern in air-water annular flows is qualitatively similar to that of heated annular flow in that the liquid film stays on the wall, enclosing a vapor core, there could be significant differences in the local variables measured due to density ratio effects. Development of mechanistic models for multi-dimensional computer codes for predicting two-phase flows in many heated systems relies on local measurements of variables in high pressure flows. Since it is difficult to measure local quantities in steam-water flows at high pressure, this paper concentrates on annular flow measurements in a refrigerant fluid, R-134a, with the same density ratio as steam-water at high pressures.

Most of the measurements available in the literature have been made for circular tubes. In rectangular geometries, for some flow conditions, the collection of liquid at the edges allows the liquid film to have different thicknesses and the roll waves to have different amplitudes. Consequently, the droplet disintegration mechanism in non-circular geometries is non-isotropic and three-dimensional. There is a need to generate such data in the literature for the development of entrainment and drop size models for non-circular geometries.

The objectives of this paper are to 1) extend the existing data base in annular flows to high pressure adiabatic, boiling flows (high vapor-to-liquid density ratios); and 2) provide detailed local measurements of void fraction, droplet frequency, droplet velocity, drop diameter and interfacial area density using hot film anemometry for a wide range of flow rates and two system pressures. Some of these measurements are used for comparison with the numerical results presented in Part II of the current paper (Kumar and Trabold, 1998). This study expands upon previous work (Trabold *et al.*, 1998) by considering two system pressures of 2.4 MPa and 1.4 MPa, and profiles across the wide test section dimension, which sheds light on the three-dimensionality of the flow in thin, high aspect ratio, vertical ducts.

Experimental Apparatus and Measurement Systems

The experimental investigation was performed to assist in developing and validating individual closure models, as well as to qualify the integrated prediction capability of the three-field approach in annular flow provided in Part II of this paper.

Test Section

The test section (Figure 1) was designed to be flat and narrow for easy optical access and to separate out edge effects. The test section has a length of 1.2 m, a cross-section aspect ratio of 22.5, and a hydraulic diameter of 4.85 mm. Optical access to the flow is provided by eight quartz windows, each 38.1 mm thick by 76.2 mm wide by 0.28m long. The center 57.2 mm of the windows comprises the transverse (*Y*) dimension of the flow duct. The working fluid used in this study is refrigerant R-134a (1,1,1,2-tetrafluoroethane) which, aside from its practical importance, is of scientific interest because of its very low liquid-to-vapor density ratio and low surface tension (i.e., 7.3 and 0.0021 N/m, respectively, at 2.4 MPa). An instrument scanning mechanism positions most of the instrumentation about the test section at any vertical, streamwise location and permits scans in a horizontal plane transverse to the test section. Two-phase annular flow was created using heaters located upstream of the test section inlet. The absence of wall vapor generation makes it easier to evaluate momentum exchange models without considering heat transfer effects.

Gamma Densitometer

A gamma densitometer system (GDS) is used to set the desired cross-section average void fraction in the test section, and also to compare the average of local void fractions obtained using the hot-film anemometer (HFA), described below. The GDS consists of a shielded 9 curie Cesium-137 source located on one side of the test section, and a Sodium Iodide (NaI) gamma detector on the other side. The gamma densitometer provides a direct density measurement of a two-phase mixture in the path of a gamma beam using the gamma beam intensities through the empty and two-phase-fluid-filled test section. The void fraction, α, at any given position through the test section is calculated from

$$\alpha = \frac{(\rho_l - \rho)}{(\rho_l - \rho_g)}. \tag{1}$$

The liquid and vapor phase densities, ρ_l and ρ_g are determined from a database for R-134a saturation properties at the measured test section exit temperature.

The gamma beam width can be changed by rotating the source collimator. The wide beam, when directed through the edge of the test section, interrogates the entire cross-section of the fluid and yields a measurement of the cross-sectional average void fraction. This measurement is first compared to the predicted average void fraction prior to comparisons of other variables. Void fraction data scans are also obtained in the narrow dimension (*Y*) using the narrow beam directed through the test section edge. These line-averaged measurements are used to compare integrated model predictions in Part II of this paper by Kumar and Trabold, 1998. Two minute counting times were used for both wide and narrow beam edge measurements. The total uncertainty, based on a root-sum-square combination of precision (random) and systematic (bias) components at 95% confidence ($\pm 2\sigma$), was determined for each type of GDS measurement. The wide beam edge measurement was obtained twice and averaged for a total uncertainty of ±0.017 in void fraction. For each narrow beam edge measurement, the total uncertainty is ±0.032.

Hot-Film Anemometer

A constant temperature hot-film anemometer (HFA) has been used previously to measure void fraction in refrigerant fluids R-113 and R-134a (Trabold *et al.*, 1994; 1997). This earlier work was extended to velocity and droplet size measurements in annular flow by Trabold *et al.* (1998).

Void Fraction:

In the current setup, a dual-sensor probe was installed at $X = 88.4$ cm (182 D_h) in the center of the width dimension of the quartz window. This HFA probe consists of two active sensing elements which are separated in the streamwise dimension by some known distance. The sensors were made of platinum with 25 μm diameter and 254 μm active length. As described in detail in the earlier publications, a combined slope and level thresholding method originally proposed by Carvalho and Bergles (1992) was used to analyze the HFA output voltage signals for determination of local vapor volume fraction. These measurements have been confirmed in bubbly, slug and annular flows through comparison between the integrated averages of local HFA data and line-average GDS measurements.

Droplet Velocity:

The use of two sensors permits acquisition of interfacial velocity measurements based on the cross-correlation between two output voltage signals. The maximum in the cross-correlation function corresponds to the most probable time required for a gas-liquid interface to travel between the HFA sensors, from which the mean interfacial velocity is calculated. The upstream sensor measures the void fraction and the droplet frequency, and the twin-sensor arrangement affords measurement of the droplet velocity.

Droplet Diameter:

In addition to the local void fraction, a measurement of local liquid droplet frequency is also obtained by counting the number of positive voltage pulses per known measurement time (Trabold *et al.*, 1998). Using the void fraction and frequency measurements from the upstream sensor, and velocity measurement from the dual sensor, the spherical equivalent droplet diameter can be calculated as

$$d_d = 1.5\frac{V_d \alpha_d}{f_d}. \tag{2}$$

Droplet size measurements were limited to test runs for which a 50 kHz digitization rate of the voltage signal was used. Droplet size calculations are not reported for narrow dimension positions (*Z* in Figure 1) where the presence of the wall and liquid film would influence the random motion of the dispersed liquid field. Since the probe position must be greater than one droplet diameter from the wall, drop diameter measurements are presented in Results and Discussion for $Z/t > 0.2$.

Interfacial Area Concentration:

The interfacial area concentration (a_i) is of central importance in modeling the thermal-hydraulic behavior of two-phase flows. This parameter corresponds to the surface area between gas and liquid phases per volume of two-phase mixture, and as such has units of inverse length. In multi-field formulations, interfacial transfer terms are described as the product of the interfacial area concentration and a driving force. For separated flows, such as the annular flows studied in the present work, quantification of a_i is complicated by the fact that two distinct fluid structures (interfacial waves and dispersed liquid droplets) contribute to the total interfacial area. The following discussion outlines how the parameters measured in the present set of experiments makes quantification of the droplet contribution to interfacial area possible, based on a set of simplifying assumptions.

Measurements of average interfacial area concentration in annular two-phase flow are quite limited and local annular flow data in rectangular geometries are nonexistent. Kataoka and Ishii (1982) characterized the average interfacial area concentration in annular flow by combining contributions from interfacial waves and dispersed droplets:

$$\bar{a}_i = \frac{4C_{an}}{D_h}\sqrt{\frac{\bar{\alpha}}{1-\bar{\alpha}_d}} + \frac{\bar{\alpha}}{1-\bar{\alpha}_d}\left(\frac{6\bar{\alpha}_d}{d_{sm}}\right) \qquad (3)$$

where C_{an} is a wave roughness parameter, $\bar{\alpha}_d$ is the average volume fraction of the dispersed droplet field and d_{sm} is the Sauter mean droplet diameter. If this expression is applied locally in the region of the flow where only the vapor core and droplets are present, the interfacial area density reduces to

$$a_i = \frac{6\alpha_d}{d_{sm}} = \frac{4f_d}{V_d}. \qquad (4)$$

For small droplets, the Sauter mean and volume equivalent diameters are approximately the same. This relation has been used for interfacial area concentration measurements in bubbly flows, based on the assumptions of spherical bubbles and bubble velocity that is constant and possesses one component of flow direction only (Galaup, 1976; Kataoka and Serizawa, 1990; Cartellier and Achard, 1991). The expression given in Equation 4 was derived by Galaup (1976) from purely geometrical considerations for bubbles in continuous liquid, and is valid for nondeformable and convex interfaces with no statistical correlation between bubble velocity and interface orientation.

Equation 4 depends upon neither the dispersed phase size distribution nor the shape. Galaup (1976) derived Eq. 4 for measurements of bubbles in air-water flows, where the characteristic size of the bubbles far exceeded the effective size of the measurement device. In the present experiments, there are conditions under which very small droplets (i.e., size of the same order as the 25 μm diameter HFA sensor) were measured and hence it is not reasonable to consider the droplets to be nondeformable. It is to be expected therefore that the largest error associated with the application of Eq. 4 will be for very small droplets, generally for average void fractions in excess of 90%. The behavior of liquid droplets upon interaction with the HFA sensor remains an open issue. Although in the process of deformation a droplet would lose some of its momentum, the generally close agreement between HFA and nonintrusive LDV velocity measurements (Trabold *et al.*, 1998) suggests that the presence of the sensor has little effect on droplet motion.

Measurement Uncertainty:

The measurement uncertainty for all reported HFA data was calculated based on the root-sum-square uncertainty interval for 95% confidence:

$$U = \pm[B^2 + (t_{95}S_{\bar{x}})^2]^{1/2} \tag{5}$$

where B is the bias limit (systematic error) and $t_{95}S_{\bar{x}}$ is the precision limit (random error). The error sources considered, and the uncertainty bands associated with local HFA measurement, are summarized in Table 1. The measurement of droplet frequency is complicated by the analysis of variable amplitude voltage signals originating from droplets of different sizes, or glancing impactions of droplets on the HFA sensor. Therefore, some of the droplets striking the sensor may not produce measurable voltage peaks, thereby biasing the frequency measurement. Because of the somewhat greater uncertainty in the frequency data, the measurements of droplet diameter and interfacial area concentration, which are inferred from frequency and other measurements, also have a relatively large uncertainty.

Flow Visualization

A high speed video (HSV) system operated at 250 frames per second was used to obtain images of the annular flow through the quartz window. Backlighting was used with a strobe light source illuminating a white diffuser. These images were used to study the behavior of the disturbance waves that appeared as dark rings, and measure their frequency and velocity for different flow conditions. At high pressure and high flows, the vapor phase is comprised of a very dense field of small and large bubbles, and their interfaces scatter the incident light resulting in undistinguishable images. Hence, use of the HSV system was generally limited to lower mass flow rates.

Results and Discussion

Detailed local measurements were obtained in annular flow of R-134a through a thin, vertical duct with an aspect ratio of 22.5. The two system pressures investigated were 1.4 and 2.4 MPa, which provided comparable density ratios as found in many practical pressurized steam-water applications. The measurements made using a dual-sensor hot-film anemometer included local void fraction, droplet frequency and velocity. The hydraulic diameter of the test section is 4.85 mm, and the wall-bounded liquid film thickness for most cases extended to less than 0.5 mm from the wall. The closest measurement point to the wall for the current measurements is 0.15 mm. Although these dimensions are small compared to the 57.2 mm width (Y) dimension of the flow duct, void profiles in the narrow (Z) dimension provide insight to the dominating flow regime transition, droplet entrainment and dryout mechanisms. Another area of modeling interest is the magnitude of drop size and interfacial area density, both of which have been inferred from the local measurements and compared with available air-water data.

One of the most significant findings from the present R-134a experimental program is that the basic structure of the phase distribution across the narrow (Z) dimension is strongly dependent upon the mass flow rate, and is for many conditions significantly different from most previously published data. Local HFA Z-dimension void fraction profiles are shown in Figure 2 for $w = 106$ kg/hr and $P = 2.4$ MPa, with the cross-sectional average void fraction varied by adjusting the power applied to heaters upstream of the test section inlet. Because of the flow symmetry, the measurements were only obtained to about duct centerline ($Z/t = 0.5$). At $\bar{\alpha} = 0.75$, the void profile is approximately parabolic as the flow undergoes transition from churn-turbulent to annular flow. As the average void fraction is increased from 0.75 to 0.85 and then to 0.92, the wall-bounded film thickness reduces, and the near-wall void fraction gradient decreases as the flatness in the profiles extends closer to the wall. The maximum local void fraction in each case increases as the average void fraction is increased as expected, but stays below 1.0 due to the presence of droplets shearing off the disturbance waves in the liquid film. The shapes of these profiles are generally consistent with most of the data published for low pressure flows, for example the air-water experiments of Jones and Zuber (1978) conducted in a 0.51 by 6.35 cm rectangular duct.

Figure 3 shows the local void fraction profiles for a higher flow rate ($w = 532$ kg/hr) at two different pressures. For these experimental test runs, the HFA hardware was modified to afford traversing of the probe beyond the duct centerline, in order to confirm the flow symmetry. These two sets of profiles are compared with one another for the same average void fraction (as indicated in the lower left corner of each figure), and each profile is compared with the line-average void fraction measured using the gamma densitometer, as indicated in each figure by a horizontal dashed line. Considering first the measurements for 1.4 MPa in Fig. 3a, as the void fraction is increased from $\bar{\alpha} = 0.7$ to 0.95, the flow appears to proceed through several distinct transitions in the two-phase flow structure. Although the $\bar{\alpha} = 0.70$ profile has the "classic" parabolic shape, similar to the $\overline{\alpha} = 0.75$ data illustrated in Figure 2, the local data for an average void fraction of 0.80 show a distinct local maximum at $Z/t = 0.8$, with an approximately 6% void fraction decrease between this location and the duct centerline. As the average void fraction is increased to 0.95, the void fraction profile becomes "inverted", with maximum void fraction near the wall and minimum void fraction at the duct centerline.

Now turning our attention to Fig. 3b for 2.4 MPa, the profiles are dramatically different from those for the lower pressure in Fig. 3a and those for the same pressure and lower flow rate in Fig. 2. These void profiles in Fig. 3b change shape from a center-peaked distribution for $\overline{\alpha}=0.5$ during transition (not shown) to a near-wall maxima as the void fraction is increased to 0.71. This behavior results from the thinning of the liquid film with increasing mass flow, and the void inversion in the middle of the test section is mainly due to the large flux of entrained droplets from the edges. The thinning of the film was also observed on the high-speed video record. As the void fraction is increased to 0.8 and then 0.88 (highest flow rate achievable for this pressure and flow rate), the inversion decreases slightly. The plots show that the magnitude of void fraction measured by HFA is significantly higher compared to the GDS cross-section average indicated by the dashed line in each figure. This suggests the presence of a thick liquid film near the two transverse (*Y*) edges. At $\overline{\alpha}=0.88$, the void profile in the vapor core is approximately flat and two-dimensional, as the liquid film is depleted around the perimeter of the cross-section. As discussed previously by Trabold *et al.* (1998), the distinct void fraction inversions measured for w = 532 kg/hr are related to the droplet entrainment mechanism. The production of dispersed droplets by shearing of the waves in the liquid film is ultimately dependent upon the liquid-to-gas density ratio, which for R-134a is 16.2 and 7.3 for P = 1.4 and 2.4 MPa, respectively. In the vast majority of experimental investigations for which local measurements are available, such as air-water and similar low pressure systems, this density ratio is on the order of 100 to 1000.

To understand the characteristics of the liquid film and the disturbance waves and other wave patterns in the annular flow field, high speed video pictures of the flow were viewed from the flat side of the test section through the quartz windows. Although the thickness of the liquid films, which are on the order of 0.15 mm to 0.5 mm for these flows, could not be directly measured, the types of wave surfaces, their velocity and frequency could be determined. At low void fractions ($\bar{\alpha} \sim 0.75$), as was noted in the center-peaked parabolic void profiles, the overall flow is still undergoing late stages of transition into the annular regime, although it is locally annular near the center. At higher void fraction ($\bar{\alpha}=0.94$), sequential video pictures (two frame images are shown in Fig. 4) show that the waves appear as dark rough patches. The wave velocity is expected to be lower near the edges and maximum near the center, and hence the waves are clearly bow-shaped. The successive disturbance waves were counted, and the distance between two waves was measured over a period of time to obtain wave velocity and frequency. For a flow rate of 106 kg/hr, the wave frequency increases from 16 Hz to 34 Hz as the void fraction is increased from 0.71 to 0.94. As the flow rate is increased to 266 kg/hr, the wave frequencies for void fractions 0.71 and 0.82 are 50 Hz and 66 Hz, respectively. Thus, in general, the wave trends observed in high pressure refrigerant flows are similar to those of air-water flows, namely, the wave frequency increases with both gas flows (through increasing void fraction) and liquid flow rates (Hall-Taylor *et al.*, 1963; Hall-Taylor and Nedderman, 1968). However, the superficial gas velocity for these cases is on the order of 1 to 2 m/sec. Compared to Okada *et al.*'s (1995) wave frequency versus superficial gas velocity plot, the frequency in the current high gas density flows is significantly higher, consistent with Gill *et al.*'s (1969) measurements in high gas density flows.

The average wave velocity measured from the video pictures for $\bar{\alpha}=0.94$ is 0.57 m/sec. For a neutrally stable film, using a simple force balance at the interface between the liquid film and the vapor core, the wave velocity can be obtained as

$$u_w = \frac{\sqrt{\frac{\rho_g}{\rho_l}}u_g + u_l}{1 + \sqrt{\frac{\rho_g}{\rho_l}}}. \tag{6}$$

The average values of vapor velocity, u_g, and liquid velocity, u_l, can be calculated using the one-dimensional relationship in terms of measured quality and mass flux as

$$u_g = \frac{x\,G}{\alpha\rho_g}\,;\; u_l = \frac{(1-x)\,G}{(1-\alpha)\rho_l}. \tag{7}$$

The wave velocity calculated using Eqs. 6 and 7 is 0.62 m/sec which compares well with the wave velocity measured from video footage.

The visualized waves are not always clearly defined in the video images. When the liquid film at the transverse (*Y*) edges is thick, as in the case of 266 and 532 kg/hr in the void fraction range of 0.85, several waves emerging from one edge are observed to only extend to the middle of the test section. These half waves are initially relatively slow but then occasionally coalesce with half waves originating from the other edge, and then travel much faster as full bow-shaped waves. These disturbance waves may approach a slow moving half wave upstream and form a λ-shaped wave. The λ-shaped waves then propagate through the film. Although this unique phenomenon has not been reported previously, it is not unlike the circumferential ring waves observed recently in air-water flows in tubes (Ohba *et al.*, 1995; Okada *et al.*, 1995), but much more distinguished and three-dimensional because of the high aspect ratio of the duct.

To develop an understanding of the effect of this observed liquid film wave behavior on the dispersed droplet field, as well as to assess the degree of three-dimensionality of the flow, a dual-sensor hot-film probe was installed between the third and fourth window elevations (i.e., between

Windows 3 and 7 and Windows 4 and 8; see Figure 1). This probe scanned across the *Y* dimension at the test section center plane (i.e., $Z/t = 0.5$). In Figure 5, local *Y*-dimension velocity data are presented for $P = 1.4$ MPa and 2.4 MPa at $w = 532$ kg/hr, the same conditions for which Z-dimension void fraction data are provided in Figure 3. The transverse velocity profiles for these two pressures exhibit a dip near the transverse test section center. This is a result of the disturbance waves that originate near the edges of the test section merging in the center and deposit a higher concentration of larger, presumably slower moving, liquid droplets. This hypothesis is strengthened by the void profiles that display a decrease in void fraction for many of the runs near the test section center, which is consistent with the video images in Fig. 4 indicating dark regions of slower moving fluid in the center.

One of the most important parameters that governs the transport process in the annular vapor core is droplet entrainment. The ratio of the liquid phase in the film to that in droplet form varies according to the fluid flow rates and the density ratio. Although no direct measurement of the entrained fraction of droplets is available for refrigerant flows in non-circular ducts, the amount of entrainment affects the void fraction distribution which can be compared with models as discussed in Part II of this paper. Among the different types of generation of droplets associated with entrainment (Hewitt and Hall-Taylor, 1970), roll wave shearing and liquid bridge disintegration mechanisms are considered most responsible in the current flow situation. Since roll waves are present both on the flat side of the walls as well as the edges, and even if the mechanism of entrainment is the same for each, the rates may be different. Since the wave patterns from the videos and the void fraction profiles suggested that the edge film is considerably thicker, it is possible that liquid bridges may exist for some flow conditions, which would disintegrate contributing to large size droplets.

The characteristics of the dispersed droplet field in the narrow (Z) dimension are captured in Figures 6 and 7 which illustrate local void fraction, droplet velocity, droplet frequency, droplet diameter and interfacial area density. The void fraction and velocity data have been qualified previously based upon comparisons to simultaneous gamma densitometer and laser Doppler velocimetry (LDV) measurements.

In Figure 6, the effect of cross-sectional average void fraction on the Z-dimension parameter distributions is illustrated for $w = 532$ kg/hr and $P = 1.4$ MPa. The void fraction data (Figure 6a) were presented previously in Figure 3a, but are included here for completeness. Despite the inversion in the local void fraction data, resulting in a local minimum at the duct centerline, the velocity (Figure 6b) increases monotonically from the measurement position nearest the wall. For the lower void fraction condition ($\overline{\alpha} = 0.80$), there is a definite change in the profile from the near-wall region ($0.9 < Z/t < 1.0$) to the central core region ($Z/t < 0.85$). For this experimental condition, it appears that the HFA probe is being traversed through the wall-bounded liquid film, into the interfacial waves, and finally into the dispersed droplet field. No such velocity trend is observed for $\overline{\alpha} = 0.95$, as the liquid film is very thin, and the HFA probe is exposed only to dispersed droplets in continuous vapor.

The local frequency measurements presented in Figure 6c show that there is an approximately 75% increase in f_d upon increasing the average void fraction from 0.80 to 0.95. The lower void fraction data display nearly constant frequency across the vapor core, while a slight maximum exists in the profile for $\overline{\alpha} = 0.95$. As given previously in Equation 2, the local droplet diameter can be calculated from measurements of void fraction, velocity and frequency, and these data are plotted in Figure 6d. From the inversion in the void fraction scans (Figure 6a), it is evident that the liquid volume fraction ($\alpha_d = 1 - \alpha$) is greatest at the duct centerline. Because the gradients in velocity and frequency are small, this volume fraction peak also leads to a peak in the local droplet diameter near the centerline. As expected, there is a significant decrease in the magnitude of the diameters as the cross-sectional average void fraction is increased from 0.80 to 0.95. As given by Equation 4, the local interfacial area concentration in the vapor core can be calculated from measurements of velocity and frequency. The data scans for two average void fraction at P = 1.4 MPa and w = 532 kg/hr are shown in Figure 6e. Because the velocity and frequency increase in similar proportions upon increasing the void fraction from 0.80 to 0.95, the net result is that the local a_i values are nearly equivalent. Also, the profiles are approximately flat over the range $0.3 < Z/t < 0.8$.

Figure 7 shows the effect of mass flow rate on the local Z-dimension parameter distributions for a fixed system pressure of 2.4 MPa and cross-sectional average void fraction of 0.94. Because of the very high average vapor volume fraction, the liquid film is quite thin and the void fraction profiles (Figure 7a) are nearly flat as the probe is traversed through the dispersed droplet field. In Figure 7b, it is seen that the local velocity increases by a factor of approximately five, which is in line with the increase in the mass flow rate from 106 to 532 kg/hr. The droplet frequency data in Figure 7c illustrate the more than ten-fold increase in droplet frequency at the higher flow rate, as well as the significant gradient in frequency between near-wall and centerline measurement locations for w = 532 kg/hr. The data in Figure 7d show a definite decrease in droplet diameter for the higher flow rate. Unlike the trend shown in Figure 6e, the interfacial area concentration is strongly dependent on mass flow rate, and apparently increases toward the duct centerline. Interfacial area concentration results are discussed further later.

Various drop size models have been discussed by Azzopardi (1997). Trabold *et al* (1998) presented drop size measurements for high pressure flows. Their measurements did not include lower pressure (still significantly higher than atmospheric pressure) cases. The objective of the current presentation of the reanalyzed droplet data is to test the available models in the literature and implement the most suitable model in the three-field code to obtain integrated predictions (Kumar and Trabold, Part II). Two models under consideration are Ueda's (1979; 1981) based on his R-113 refrigerant data, and a more mechanistically based model by Kocamustafaogullari *et al.* (1994). By introducing the vapor-to-liquid density ratio, a correlation was derived to describe data for a variety of fluids, including R-113, water and aqueous glycerol solutions:

$$\frac{d_m}{D_h} = 5.8 \times 10^{-3}\left[\frac{\sigma}{\mu_g U_g}\left(\frac{\rho_g}{\rho_l}\right)^{1.25}\right]^{0.34} = 5.8 \times 10^{-3} R^{0.34} \qquad (8)$$

where d_m is the volume weighted droplet diameter.

A comparison of the mean R-134a droplet diameter measurements (averaged from the presented profiles) and the correlation of Ueda (1979) is illustrated in Figure 8. The parameter R was calculated using R-134a physical properties at saturation pressures of 1.4 and 2.4 MPa. Included in Figure 8 are the air-water data of Wicks and Dukler (1966), which were also obtained in a rectangular duct. It is evident that the Ueda droplet size relation underpredicts much of the R-134a data, as well as most of the data of Wicks and Dukler.

The second model considered is by Kocamustafaogullari *et al.* (1994) who developed an expression for the Sauter mean droplet diameter, by considering the maximum stable droplet size in the turbulent vapor core:

$$\frac{d_{sm}}{D_h} = 0.65 C_w^{-\frac{4}{15}} We_m^{-\frac{3}{5}} \left(\frac{Re_g^4}{Re_l}\right)^{\frac{1}{15}} \left[\left(\frac{\rho_g}{\rho_l}\right)\left(\frac{\mu_g}{\mu_l}\right)\right]^{\frac{4}{15}} \left(\frac{\Delta\rho}{\rho_l}\right)^{-\frac{3}{5}} = 0.65K \qquad (9)$$

where:

$$C_w = \frac{1}{35.34 N\mu^{0.8}} \quad for\ N\mu \le \frac{1}{15} \qquad (10)$$

$$N\mu = \textit{viscosity number} = \frac{\mu_f}{\left[\rho_f \sigma \left(\frac{\sigma}{g\Delta\rho}\right)^{\frac{1}{2}}\right]^{\frac{1}{2}}} \tag{11}$$

$$We_m = \textit{modified Weber number} = \frac{\rho_g D_h \langle j_g \rangle^2}{\sigma} \tag{12}$$

and the gas Reynolds number (Re_g) and liquid Reynolds number (Re_l), are based on the phasic superficial velocities. In Figure 9, the mean R-134a droplet diameter data obtained at P = 1.4 and 2.4 MPa are compared with the relation of Kocamustafaogullari *et al.* (Equation 10) and the rectangular duct data of Wicks and Dukler (1966). It should be noted that the factor $(\Delta\rho/\rho_l)^{-3/5}$ appears on the right-hand side of Equation 9 based on the original derivation for fluids having small density ratios. For high pressure (2.4 MPa), this factor increases droplet diameter by more than 9%. The data plotted in Figure 9 show some scatter about the line representing Equation 9, but this relation reasonably describes the overall trend in the data. This is significant because of the wide variety of fluid physical properties, gas and liquid flow rates and duct geometries investigated, and the various measurement techniques employed. Perhaps the most encouraging aspect of this data comparison is that the liquid-to-gas density ratio varied from 7.3 for R-134a to 3700 in the helium-water experiments of Jepson *et al.* (1989).

In Part II of this paper (Kumar and Trabold, 1998), Ueda's (1981) model has been chosen for its simplicity, ease of local implementation (no global physical parameters), and because both experiments were conducted for fluids having a relatively low surface tension and high vapor-to-liquid density ratio. The hot-film anemometer probe may not measure all droplets which strike the sensor, and hence bias the size measurement toward larger droplets. Therefore, it is assumed that the measured droplet size may be better represented by the volume weighted diameter defined in Equation 9. The few data points from the current experiments which are well predicted by the

Ueda relation in Figure 8 also correspond to a majority of the modeling conditions, namely, $\overline{\alpha} > 0.9$.

Now, more attention is paid to interfacial area concentration profiles illustrated in Figures 6e and 7e. Once again, this calculation is limited to regions of the flow for which the hot film results showed close agreement with simultaneous LDV measurements (Trabold *et al.*, 1998). The local interfacial area concentration falls within a fairly narrow range along the narrow Z-dimension. This result is not surprising since most droplet frequency and droplet velocity profiles were flat in the vapor core. The local measurements acquired for each experiment were spatially averaged, and the results are presented in Figure 10 to demonstrate the variation with average void fraction. Several points can be made from this figure. For the same void fraction and system pressure, as the mass flow rate is increased, the interfacial area concentration increases. For the same flow rate of 532 kg/hr, as the pressure is increased from 1.4 MPa to 2.4 MPa, the interfacial concentration increases. The distribution of interfacial area with void fraction is relatively flat within the experimental uncertainty.

As documented by Ishii and Mishima (1981), most data available for interfacial area concentration, a_i, correspond to air-water flows in circular pipes. The largest average interfacial area concentration reported in such flows is 25 cm^{-1} measured at a gas superficial velocity of 37 m/sec (Wales, 1966). For many of the test conditions covered in the present study, the average a_i significantly exceeds this value even though the maximum gas superficial velocity was only 7.2 m/s.

The wide variations between the present R-134a experiments and those available in air-water may be related to two key parameters: the fraction of entrained liquid and the mean liquid droplet size. For a given quality, the entrainment fraction corresponds to the mass fraction of the liquid phase that is contained in the dispersed droplet field. Liquid in the form of dispersed droplets would contribute more to the interfacial area than if flowing as part of the liquid film. A large value of entrainment fraction would, of course, correspond to a large average droplet volume fraction, $\overline{\alpha}_d$. For a representative pipe diameter of 1 cm and volume mean droplet diameter of 500 µm, Ishii and Mishima developed a plot of the characteristic interfacial area concentrations for variations in both average void fraction, $\overline{\alpha}$, and average droplet volume fraction, α_{fd}. For many of the present experiments, both the local void fraction profiles and high-speed video records suggest the presence of a thin liquid film. Therefore, much of the liquid phase is contained within the liquid droplets, thereby increasing the value of α_{fd} and the expected range of average interfacial area concentrations.

For a given volume of liquid, the interfacial area is greater for a larger number of small droplets. Therefore, an inverse functionality exists between a_i and the droplet diameter, as described by Equation 4. The ratio of expected droplet size in an air-water flow through a 1 cm diameter pipe to that in TF-116 can be estimated by invoking the correlation of Ueda (1981). For a given gas superficial velocity, Equation 8 yields

$$\frac{d_{R-134a}}{d_{air-water}} = \frac{\left\{D_h\left[\frac{\sigma}{\mu_g}\left(\frac{\rho_g}{\rho_l}\right)^{1.25}\right]^{0.34}\right\}_{R-134a}}{\left\{D_h\left[\frac{\sigma}{\mu_g}\left(\frac{\rho_g}{\rho_l}\right)^{1.25}\right]^{0.34}\right\}_{air-water}} . \tag{13}$$

Substitution of the appropriate physical property and hydraulic diameter information yields a diameter ratio of 1.1 for R-134a at 2.4 MPa and 1.25 at 1.4 MPa. Hence, the expected droplet size for R-134a is of the same order of magnitude as a typical air-water flow for which interfacial area concentration data are reported. It may therefore be concluded that the higher interfacial area concentration in the refrigerant flow is primarily a result of a larger entrainment fraction.

Conclusions

Detailed local measurements of void fraction, droplet frequency, velocity, mean drop size and interfacial area concentration have been obtained using a hot-film anemometer in annular flow through a vertical duct. These measurements improve the current understanding of physical mechanisms, as well as extend the existing data base in low liquid-to-vapor density ratio flows. The line-averaged void fraction and the droplet velocity measurements have been primarily obtained to validate the integrated effects of the models in Part II of this work. By making measurements in both coordinates of the cross-section, it has been shown that even in vertical flows for an aspect ratio of 22.5, the flow can be three-dimensional with a large flux of entrained droplets from the edges. These droplets lead to an inversion in the void fraction, which is predominant for void fraction less than 0.9 for almost all flow rates. The flow is three-dimensional for void fractions much less than 0.9 and high flow rates. Corresponding to the void profiles, the droplet diameter profiles increase or decrease toward the center of the duct depending on the average void fraction and the flow rate. The average droplet diameter agrees well for both system pressures with the model proposed by Kocamustafaogullari *et al.* (1994) when the lower liquid-to-vapor vapor density ratio is taken into account. Interfacial area concentration increases with flow rate and pressure, and is found to be significantly higher compared to similar measurements made in air-water flows. This appears to be due to a larger entrainment fraction in the low density ratio refrigerant flows.

The wave patterns have been analyzed using high speed photography, and the wave velocity measured by wave counting matches reasonably well with one-dimensional models for neutrally stable film. Disturbance waves are bow-shaped when two-dimensional as is usually observed in circular tubes, and λ-shaped when three-dimensional. These limited measurements suggest that the wave frequency increases with both gas flows (through increasing void fraction) and liquid flow rates as reported by Hall-Taylor *et al.* (1963) and Hall-Taylor and Nedderman (1968) in air-water flows, and with gas density as reported by Gill *et al.* (1969).

Acknowledgements

The authors gratefully acknowledge Messrs. W.O. Morris and L. Jandzio for their efforts in the operation of the test facility, Mr. D.M. Considine for his efforts in flow visualization and Dr. G.J. Kirouac for his direction of the experimental program.

References

Azzopardi, B.J. (1997) "Drops in Annular Two-Phase Flow," *Int. J. Multiphase Flow*, Vol. 23, Suppl., pp. 1-53.

Cartellier, A. and Achard, J.L. (1991)"Local Phase Detection Probes in Fluid/Fluid Two-Phase Flows," *Review of Scientific Instruments*, Vol. 62, pp. 279-303.

Carvalho, R. and Bergles, A.E. (1992) "The Pool Nucleate Boiling and Critical Heat Flux of Vertically Oriented, Small Heaters Boiling on One Side," Rensselaer Polytechnic Institute, Heat Transfer Laboratory Report HTL-12, August.

Galaup, J.P. (1976) "Contribution to the Study of Methods for Measuring Two-Phase Flow," Centre D'Etudes Nucleaires de Grenoble, Report No. 136.

Gill, L.E., Hewitt, G.F. and Roberts, D.N. (1969) "Studies of the behavior of disturbance waves in a long vertical tube," UKAEA Report AERE R6012.

Hewitt, G.F. and Hall-Taylor, N.S. (1970) *Annular Two-Phase Flow*, Pergamon Press.

Hall-Taylor, N.S., Hewitt, G.F. and Lacey, P.M.C. (1963) "The Motion and Frequency of Large Disturbance Waves in Annular Two-Phase Flow of Air-Water Mixtures," Chem Engng Sci., Vol. 18, pp. 537-552.

Hall-Taylor, N.S. and Nedderman, R.M. (1968) "The Coalescence of Disturbance Waves in Annular Two-Phase Flow," Chem. Engng Sci., Vol. 23, pp. 551-564.

Ishii, M. and Mishima, K. (1981) "Study of Two-Fluid Model and Interfacial Area," Argonne National Laboratory Report ANL-80-111.

Jepson, D.M., Azzopardi, B.J. and Whalley, P.B. (1989) "The Effect of Gas Properties on Drops in Annular Flow," *Int. J. Multiphase Flow*, Vol. 15, pp. 327-339.

Jones, O.C. and Zuber, N. (1978) "Use of a Cylindrical Hot-Film Anemometer for Measurement of Two-Phase Void and Volume Flux Profiles in a Narrow Rectangular Channel," *Heat Transfer: Research and Application,* AIChE Symposium Series, Vol. 74, No. 174, pp. 191-204.

Kataoka, I. and Ishii, M. (1982) "Mechanism and Correlation of Droplet Entrainment and Deposition in Annular Two-Phase Flow," Argonne National Laboratory Report ANL-82-44.

Kataoka, I. and Serizawa, A. (1990) "Interfacial Area Concentration in Bubbly Flow," *Nuclear Engineering and Design*, Vol. 120, pp. 163-180.

Kocamustafaogullari, G., Smits, S.R. and Razi, J. (1994) "Maximum and Mean Droplet Sizes in Annular Two-Phase Flow," *Int. J. Heat Mass Transfer*, Vol. 37, pp. 955-965.

Kumar, R. and Trabold, T.A. (1998) "High Pressure Annular Flow in a Narrow Duct. Part II: Three Field Modeling," submitted for publication in *ASME J. Fluids Eng.*

Ohba, K., Nakamura and Naimi, F. (1995) "A New Kind of Interfacial Wave on Liquid Film in Vertically Upward Air-Water Two-phase Annular Flow," Proc. 2nd Int. Conf. on Multiphase Flow, Paper IP1, pp. 27-33.

Okada, O., Fujimatsu, T., Fujita, H. and Nakajima, Y. (1995) "Measurement of Droplet Size Distribution in an Annular Mist Flow in a Vertical Pipe by Immersion Liquid Method," Proc. 2nd Int. Conf. on Multiphase Flow, Paper IP2, pp. 11-18.

Trabold, T.A., Moore, W.E., Morris, W.O., Symolon, P.D., Vassallo, P.F. and Kirouac, G.J. (1994) "Two Phase Flow of Freon in a Vertical Rectangular Duct. Part II: Local Void Fraction and Bubble Size Measurements," *Experimental and Computational Aspects of Validation of Multiphase Flow CFD Codes*, I. Celik *et al.* (Ed.), FED-Vol. 180, pp. 67-76, ASME.

Trabold, T.A., Moore, W.E. and Morris, W.O. (1997) "Hot-Film Anemometer Measurements in Adiabatic Two-Phase Refrigerant Flow through a Vertical Duct," ASME Fluids Engineering Division Summer Meeting, Vancouver, B.C., Paper FEDSM97-3518.

Trabold, T.A., Kumar, R. and Vassallo, P.F. (1998) "Annular Flow of R-134a in a Vertical Duct: Local Void Fraction, Droplet Velocity and Droplet Size Measurement," accepted for presentation at ASME IMECE'98, Anaheim, CA.

Ueda, T. (1979) "Entrainment Rate and Size of Entrained Droplets in Annular Two-Phase Flow," *Bull. JSME*, Vol. 22, pp.1258-1265.

Ueda, T. (1981) "On the Droplets Entrained in Two-Phase Annular and Mist Flows," *Two-Phase Flow Dynamics*, A.E. Bergles and S. Ishigai (eds.), Hemisphere, pp. 75-93.

Wales, C.E. (1966) "Physical and Chemical Absorption in Two-Phase Annular and Dispersed Horizontal Flow," *AIChE Journal*, Vol. 12, pp. 1166-1171.

Wicks, M. and Dukler, A.E. (1966) "In Situ Measurements of Drop Size Distribution in Two-Phase Flow - A New Method for Electrically Conducting Liquids," *Proc. of the 3rd Int. Heat Transfer Conf.*, Vol. 5, pp. 39-49.

Table 1 - Uncertainty Bands for Measurements with Hot-Film Anemometer

void fraction	• repeatability based on pooled standard deviation • biases: threshold voltage, small droplets, test section position, sampling time	±0.025
droplet frequency	• same as void fraction • also, droplet impaction bias	-79 to +90 Hz at w = 106 kg/hr -321 to +652 Hz at w = 532 kg/hr
droplet velocity	• repeatability • biases: velocity sampling, droplet size, cross-correlation, sensor spacing, test section position	-7.5% to +7.0% (near wall) -7.0% to +6.4% (far wall)

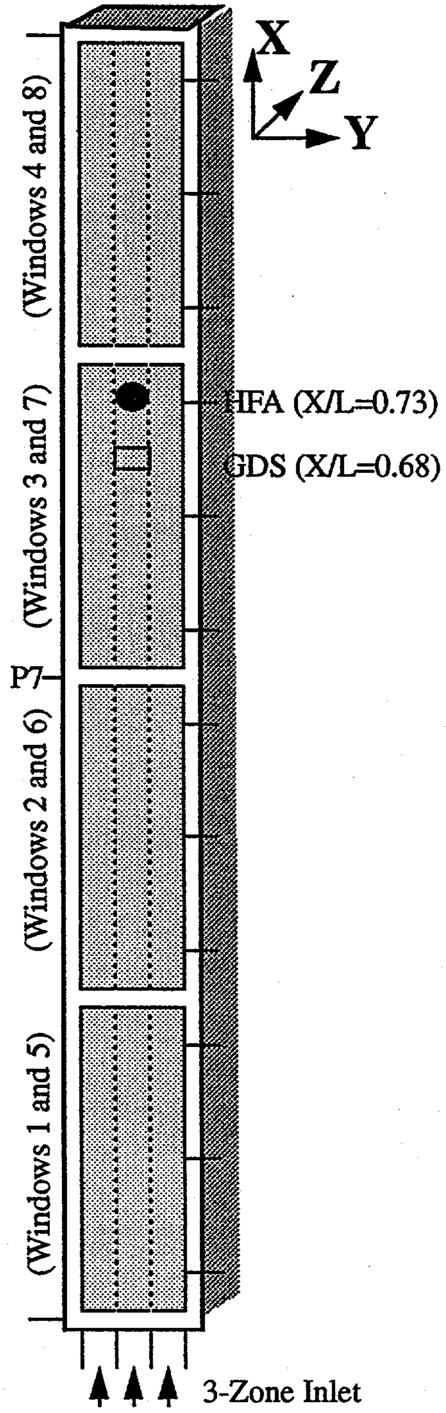

Figure 1 - Front View of the R-134a Test Section and Measurement Locations

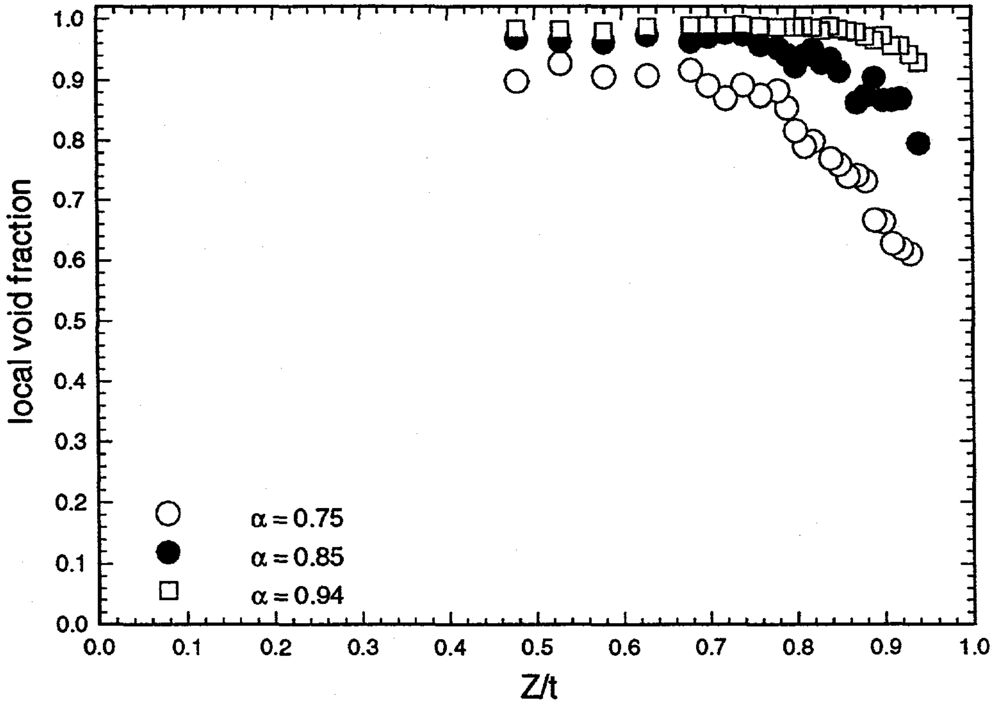

Figure 2 - Local Z-Dimension Void Fraction Distributions for w = 106 kg/hr and P = 2.4 MPa

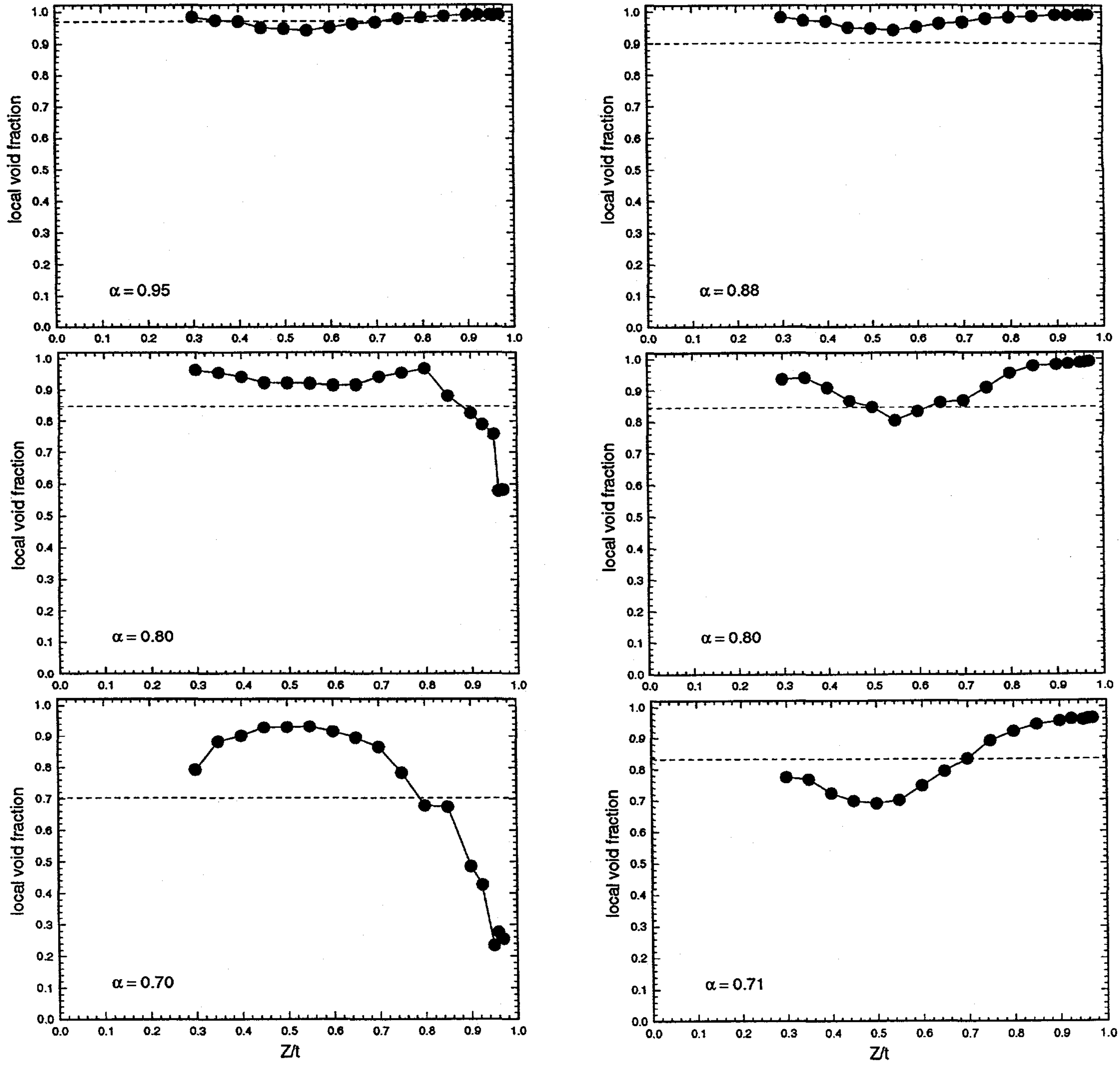

(a)

(b)

Figure 3 - Local HFA *Z*-Dimension Void Fraction Profiles for $w = 532$ kg/hr (a) $P = 1.4$ MPa; (b) $P = 2.4$ MPa. Dashed line is the cross-section average void fraction using the gamma densitometer.

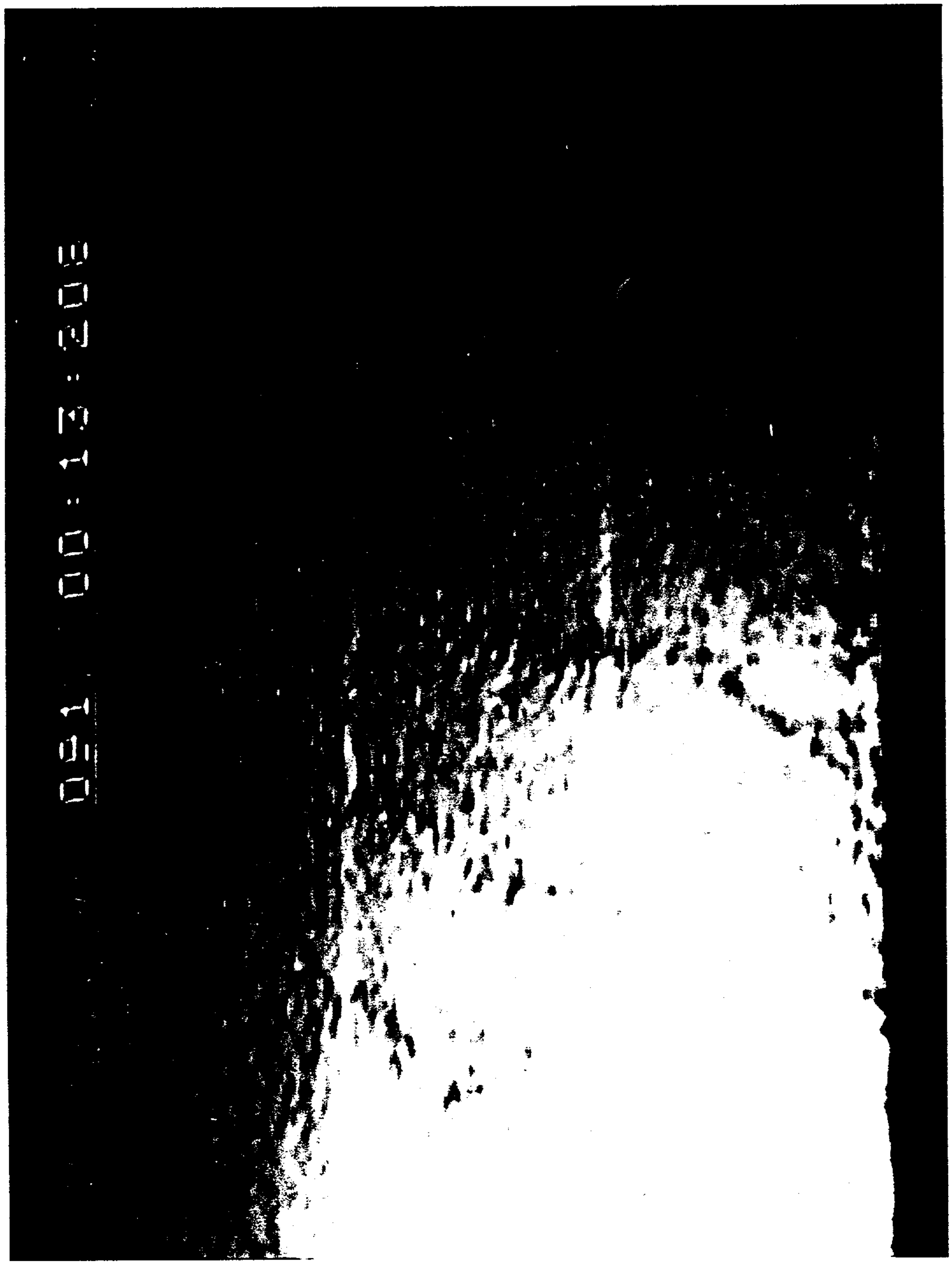

Figure 4 - Photographs of Waves in Annular Flow

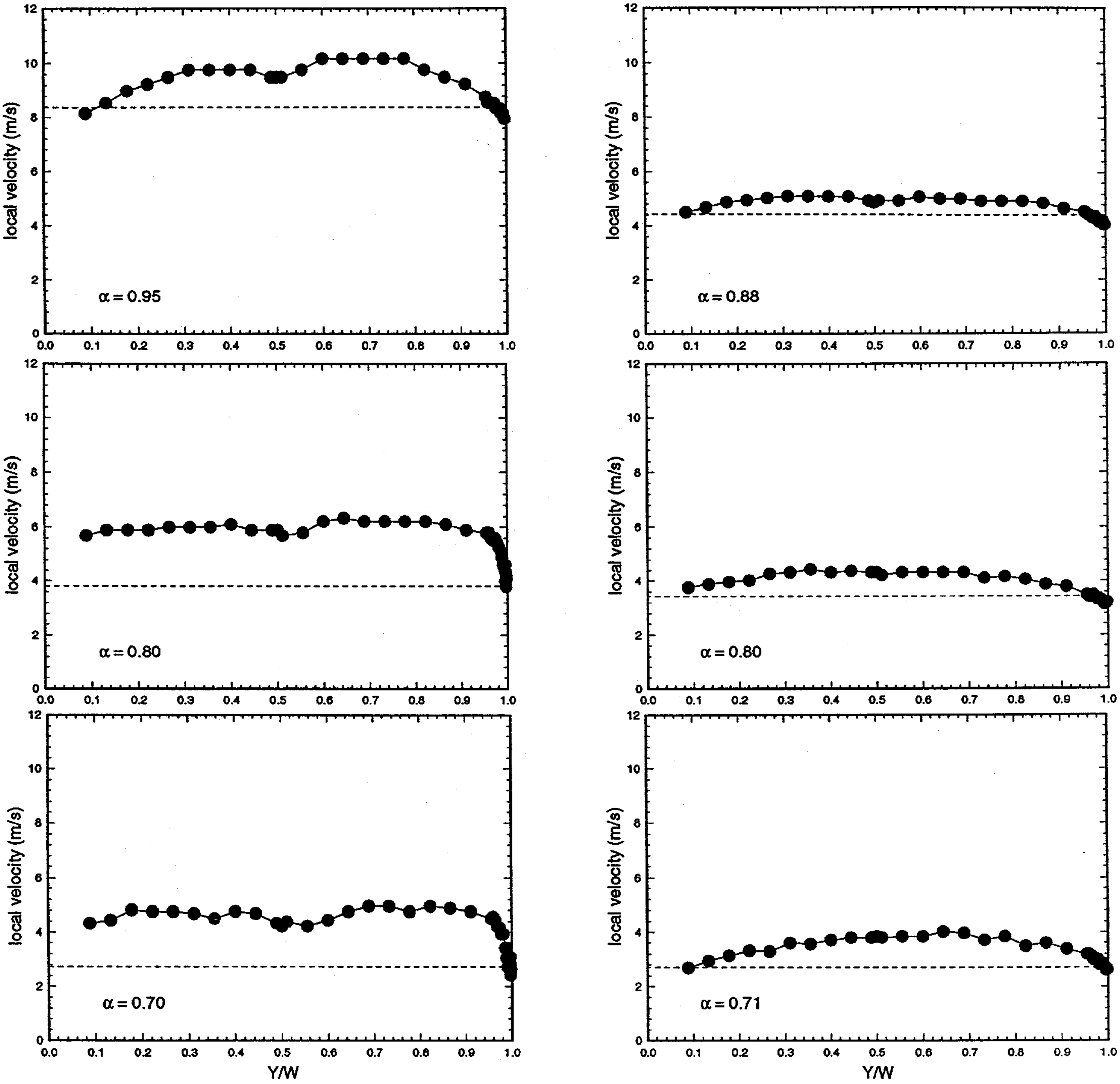

(a)

(b)

Figure 5 - Local *Y*-Dimension Velocity Profiles for $w = 532$ kg/hr (a) $P = 1.4$ MPa; (b) $P = 2.4$ MPa. Dashed line is the cross-section average void fraction using the gamma densitometer.

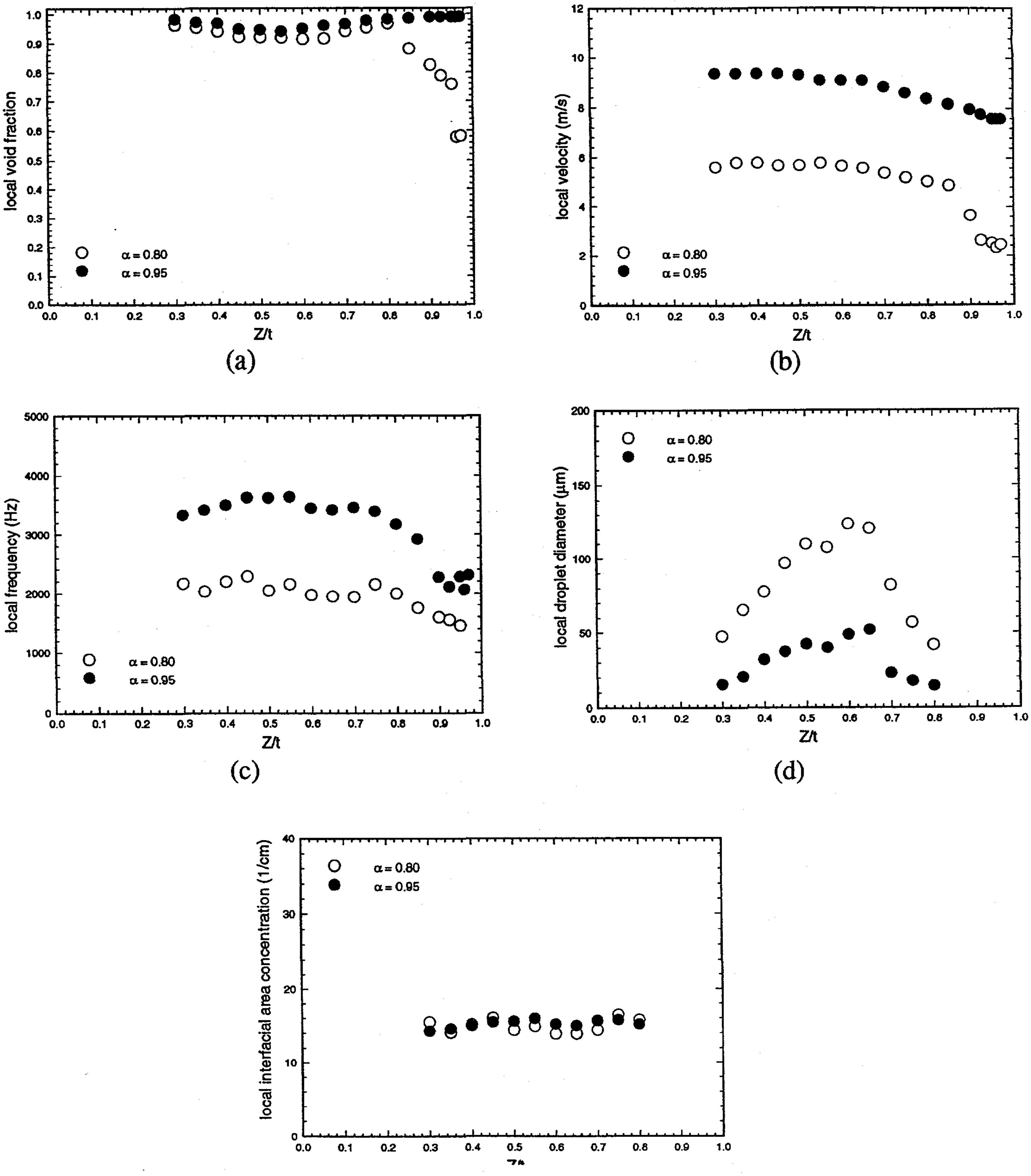

(a) (b)

(c) (d)

(e)

Figure 6 - Local Z-Dimension Parameter Distributions for $w = 532$ kg/hr and $P = 1.4$ MPa
(a) void fraction; (b) velocity; (c) frequency; (d) droplet diameter; (e) interfacial area concentration

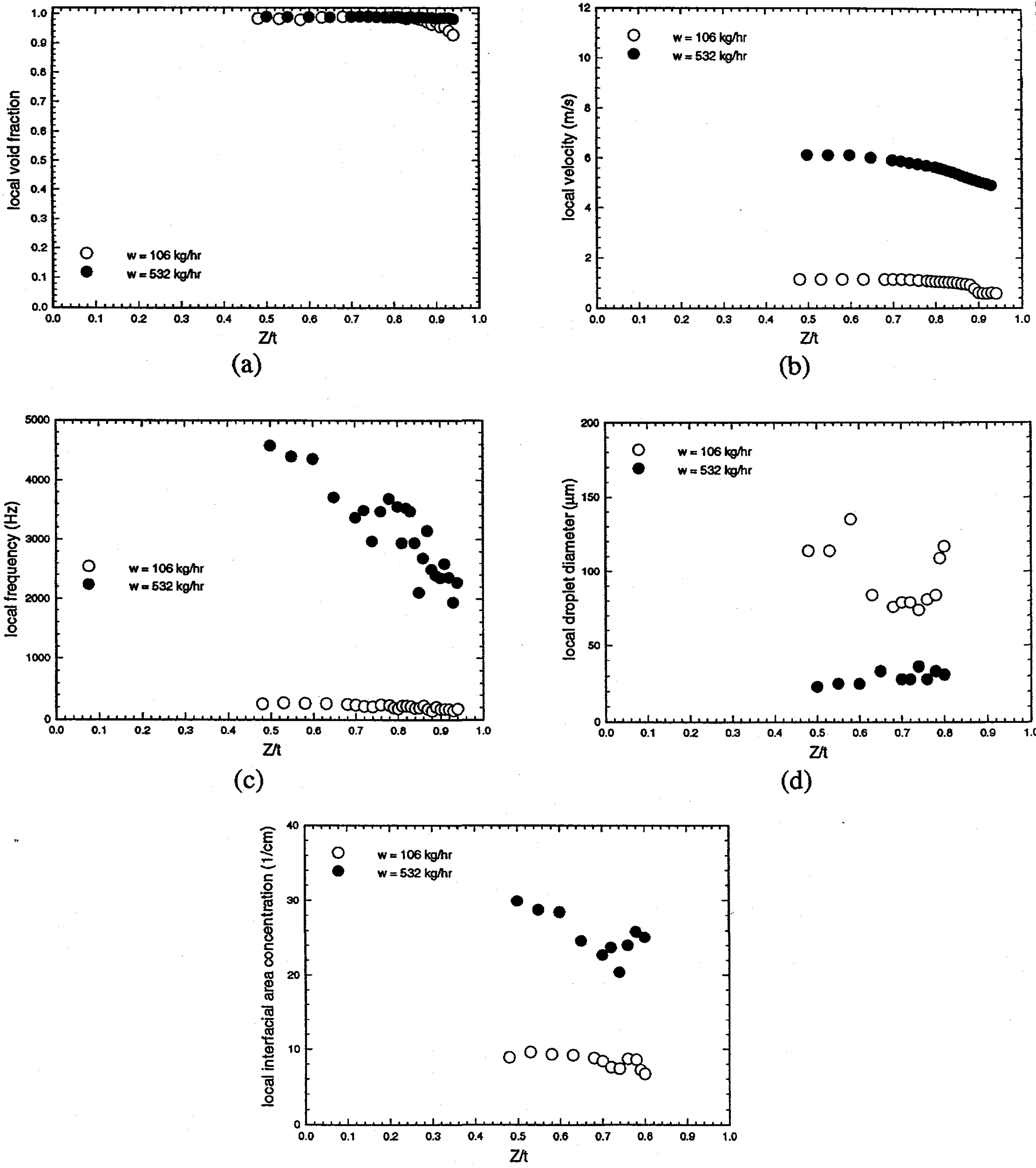

(a)

(b)

(c)

(d)

(e)

Figure 7 - Local Z-Dimension Parameter Distributions for $\alpha = 0.94$and $P = 2.4$ MPa
(a) void fraction; (b) velocity; (c) frequency; (d) droplet diameter; (e) interfacial area concentration

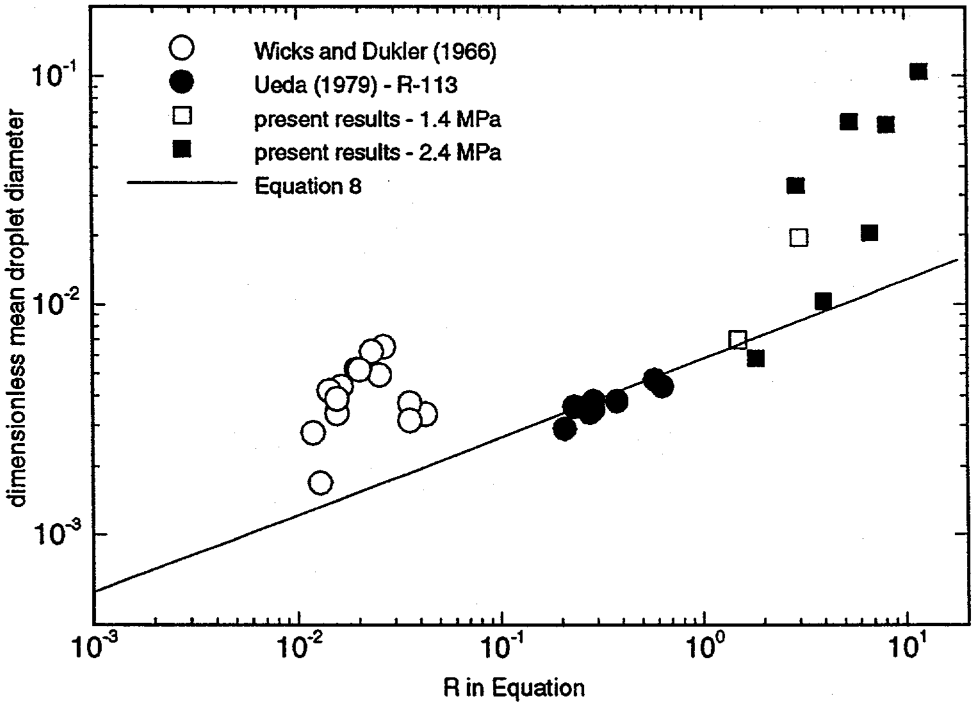

Figure 8 - Comparison of Droplet Diameter Data to Relation of Ueda (1979)

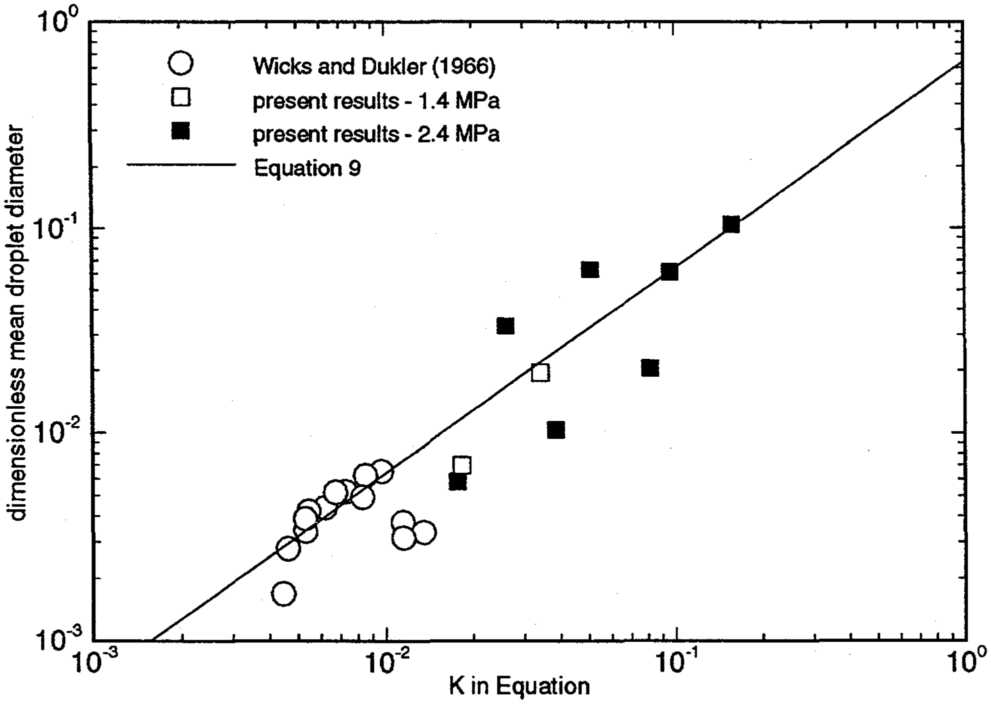

Figure 9 - Comparison of Droplet Diameter Data to Relation of Kocamustafaogullari *et al.* (1994)

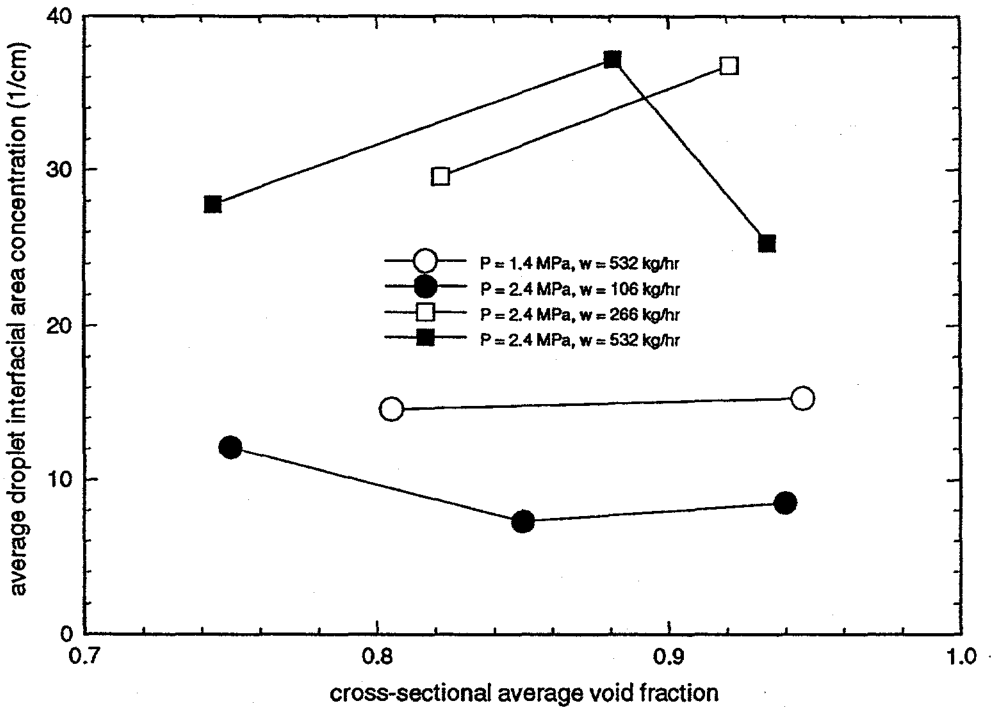

Figure 10 - Relationship Between Average Void Fraction and Interfacial Area Concentration for *P* = 1.4 and 2.4 MPa

High Pressure Annular Two-Phase Flow in a Narrow Duct. Part II: Three-Field Modeling

Ranganathan Kumar and Thomas A. Trabold
Lockheed Martin Corporation
Schenectady, NY 12301

ABSTRACT

This paper outlines the development of a three-field modeling approach in annular flow and the predictive capability of an analysis code. Models have been developed here or adapted from the literature for the thin film near the wall as well as the droplets in the vapor core, and have been locally applied in a fully developed, two-phase adiabatic boiling annular flow in a duct heated at the inlet at high pressure. Numerical results have been obtained using these models that are required for the closure of the continuity and momentum equations. The two-dimensional predictions are compared with local void fraction and droplet velocity (using a hot film anemometer), and average void fraction (using gamma densitometry) for a refrigerant fluid flowing in a narrow vertical duct with a cross-section aspect ratio of 22.5. Predicted results match the experimental data well for high void fraction annular flows, validating the overall modeling approach.

Nomenclature

A'''	Interfacial area density, 1/m
d_D	Droplet diameter, m
D_h	Hydraulic diameter, m
f	Liquid bridge breakup frequency
f_i	Interfacial friction factor
f_{sp}	Single-phase friction factor
G	Mass flux, kg/hr/m^2
k	Kinetic energy
k_s	Wall roughness, m
M_i	Non-drag force in i-field
p	pressure, Pa
P	Turbulence Production term
Re	Reynolds number
t	Duct thickness, m
u	Axial velocity, m/sec
u^*	Friction velocity, m/sec
u_R	Relative velocity, m/sec
$\underline{v}$	Velocity vector
w	Mass rate of flow, kg/hr
We	Weber number
x_i	Inlet quality
y, Y	Thickness dimension, m

Symbols

α	Void fraction
δ	Liquid film thickness
μ	Dynamic viscosity
ν	Kinematic viscosity
ρ	Density
τ_w	Shear stress
$\underline{\tau}_i$	Shear stress tensor in i-field
$\underline{\tau}_i^{Re}$	Reynolds stress tensor in i-field

$\Delta\rho$	Change in density from vapor to liquid phase
Γ_{ij}	Interfacial mass transfer rate from field i to j
ε	Turbulent energy dissipation

Subscripts and superscripts

cv	Continuous vapor field
cl	Continuous liquid field
dl	Dispersed liquid field
g	gas
f, l	liquid

Introduction

Annular flow research is the most challenging among all the flow regimes in two-phase flows because liquid exists as both continuous film and droplets. This regime is also the most important because it is usually a precursor to wall dryout. Annular flow usually occurs through a transition from the slug/churn turbulent flow regimes at high void fractions. It presents a complicated pattern of liquid phase in the form of a base film, disturbance waves and droplets, separated by a vapor core. The interface between the thin liquid film and the vapor core is characterized by a wavy motion. There are generally two types of waves: the high amplitude, low wavelength disturbance or roll waves, and the low amplitude, high wavelength ripple waves, which act to both increase the interfacial shear stress and introduce droplets into the gas core. There can also be gas entrainment in the liquid film. Hall-Taylor *et al.* (1963) and Hewitt and Hall-Taylor (1970) discuss the physical mechanisms that occur in annular flow and the physical models that describe these mechanisms.

The random motion of the waves presents some special problems in annular flow modeling and measurements that are not present in bubbly flows. These waves affect the interfacial shear stress, droplet motion, deposition and entrainment rates. These complexities have been individually modeled by various authors. Numerous papers have appeared in the literature that attribute the increase in interfacial shear in annular flow to the wave motion. Progress in modeling interfacial shear can be traced from a simple correlation between the film thickness and the interfacial friction factor [Wallis (1969)] to a law-of-the-wall approach [Hewitt and Govan (1990)] to introducing wave and turbulence characteristics [Kang and Kim (1993)]. Similarly, a number of papers have dealt with the droplet motion in the turbulent vapor core, and in particular, the drop size and entrainment and deposition of droplets [Cousins and Hewitt (1968), Kataoka, *et* *al.* (1983), Ueda(1979), and Azzopardi and Teixeira (1994)].

These papers and many others contributed significantly to two-phase annular flow modeling and experimental data base. These models capture the features of the vapor core separated by a convoluted interface, and together they contribute to the appropriate distribution and motion of the droplets in the vapor core. However, such an integrated effect of these physical mechanisms has not been numerically modeled in annular flows to date.

The current paper discusses the methodology and solutions to ensemble-averaged transport equations that describe the two-phase annular flow. An averaging process [Drew (1992)] is used to derive a system of governing equations to describe the macroscopic flow phenomenon. As done in capturing the turbulence characteristics, the averaging process usually filters out the details of the flow fields; and, therefore, additional closure equations or models need to be introduced. In the traditional two fluid approach, the liquid and vapor phases are treated separately with a set of governing equations attributed to each phase. By contrast, a four-field approach as presented by Siebert, *et al.* (1995) is used to subdivide the flow further into fields rather than phases. These idealized fields are: dispersed vapor field (dv), continuous liquid (cl), dispersed liquid (dl) and continuous vapor (cv). Within each continuous field, a dispersed field of the opposite phase can exist.

This paper has three specific objectives. 1) An ensemble averaging approach is used in a three-field framework and applied in a two-dimensional analysis code. Since the flow is annular and no heating is applied on the wall, dispersed vapor (dv) field is not created, and in effect, only three fields are used in the current flow situation. 2) Mechanistically based models are developed or currently available models are adapted from the literature for closure of the governing equations. Specifically, interfield (entrainment and deposition) models, interphase (interfacial shear) models, and other force models are locally applied to appropriately separate the liquid film from the vapor core, and to capture the physics of the droplet motion. 3) Predictions are compared with measurements obtained using hot film anemometry and gamma densitometry for different flow rates and two system pressures in a refrigerant fluid, R-134a (SUVA), at elevated temperature and pressure conditions. Emphasis is placed on the analysis of vapor fraction in the continuous vapor field and velocity in the dispersed liquid field. Shortcomings of modeling are discussed.

Governing Equations

Drew (1992) described a fundamental interpretation of time and space averages by defining the ensemble average based on the probability of a process occurring among a set of processes. To ensemble average the governing set of equations, a phase indicator function, X_k, is introduced as:

$$X_k(x,t) = \begin{cases} 1 & \text{if phase k at x,t} \\ 0 & \text{otherwise} \end{cases} . \tag{1}$$

The average of the phase indicator function, X_k, is the volume fraction of phase k, α_k, and the normal derivative of this phase indicator function is the interfacial area density. All the remaining variables are weighted averages as

$$\bar{\rho}_k = \frac{\overline{\rho_k X_k}}{\overline{X_k}} = \frac{\overline{\rho_k X_k}}{\alpha_k} \text{, and} \tag{2}$$

$$\bar{f}_k = \frac{\overline{f_k X_k \rho_k}}{\alpha_k \bar{\rho}_k} . \tag{3}$$

To perform the ensemble averaging process, the conservation equations and interface jump conditions are each multiplied by the phase indicator function, X_k, and then the equation is averaged using Eqs. (2) and (3). The final forms of the ensemble-averaged phasic governing equations can be written for any number of fields present in the flow. The predictive capability in the annular flow regime with no wall heating can be improved by an optimum number of three idealized fields: continuous liquid (cl), continuous vapor (cv) and dispersed liquid (dl). The dl-field is contained within the cv-field, and the cl-field is separated from the cv-field. The transfer of mass between fields (cl-dl and dl-cl) occurs through the hydrodynamic mechanisms of liquid bridge breakup, entrainment and deposition. This redistribution of mass among the different fields provides the predictive capability to handle flow regime transitions as continuous events rather than as discrete events. The governing equations for the three fields are given in the following Cartesian tensor form.

Conservation of phasic mass

$$\frac{\partial}{\partial t}(\alpha_i\rho_i) + \nabla\bullet(\alpha_i\rho_i\underline{v}_i) = \sum_{j\neq i}(\Gamma_{ji}-\Gamma_{ij}) \tag{4}$$

Conservation of phasic momentum

$$\begin{aligned}\frac{\partial}{\partial t}(\alpha_i\rho_i\underline{v}_i) + \nabla\bullet(\alpha_i\rho_i\underline{v}_i\underline{v}_i) &= -\alpha_i\nabla p_i - \underline{\tau}_i\bullet\nabla\alpha_i + \nabla\bullet\alpha_i(\underline{\tau}_i + \underline{\tau}_i^{Re})\\ &\quad + \underline{M}_i + \sum_{j\neq i}[D_{ij}(\underline{v}_j-\underline{v}_i) + \Gamma_{ji}\underline{v}_i - \Gamma_{ij}\underline{v}_i]\end{aligned} \tag{5}$$

Volume fraction constraint:

$$\sum_i \alpha_i = 1; \qquad 0 \le \alpha_i \le 1 \tag{6}$$

Here, subscript *i* denotes the field under consideration (i = cl, dl, cv). In the presence of three fields, there are only two admissible interfaces: cv-cl, and cv-dl. The dv-cl interface is not admitted or discussed in this paper. A double subscript denotes a quantity transferred from the field indicated by the first index (donor phase) to the field indicated by the second index (receptor phase). Γ represents the interfacial mass transfer rate between fields due to entrainment and deposition. $D_{ij}(\underline{v}_j - \underline{v}_i)$ represents the interfacial drag force between fields, and $\underline{M}_i$ represents non-drag interfacial forces between fields.

The phases are coupled via interfacial transfer terms (underlined in Eqs. 4 and 5), and jump conditions are used to relate the transfer of mass, momentum, and energy across the interface. The continuity jump condition requires zero mass accumulation on the interface. The momentum jump condition dictates that the net force acting on the interface is balanced by surface tension effects. In drag-like terms, the velocity difference across the interface is equal to the difference between the phasic velocities; but in mass transfer terms, the mass is assumed to depart the donor phase at the donor phase velocity and arrive in the receptor phase with that same velocity.

k-ε Transport Equations

The form of the k-ε transport equations used here is a simple extension of the steady state single phase model to two-phase flows. These transport equations are used only for the continuous liquid (cl) and continuous vapor (cv) fields. The production terms are refined in the wall node for annular flows as will be described in the modeling section. The dissipation of kinetic energy, ε, is calculated from the transport equation for turbulent dissipation.

Kinetic Energy Equation:

$$\nabla\cdot(\rho_i\alpha_i\underline{v}_i k_i) = \nabla\cdot\left\{\alpha_i\left(\mu_i+\frac{\mu_i^T}{\sigma_k}\right)\nabla k_i\right\}+P_i-\rho_i\alpha_i\varepsilon_i \qquad (7)$$

where

$$P_i = \alpha_i\mu_{eff}\nabla u_k\cdot(\nabla u_k+\nabla u_k^T)\ . \qquad (8)$$

Kinetic Energy Dissipation Equation:

$$\nabla\cdot(\rho_i\alpha_i\underline{v}_i\varepsilon_i) = \nabla\cdot\left\{\alpha_i\left(\mu_i+\frac{\mu_i^T}{\sigma_\varepsilon}\right)\nabla\varepsilon_i\right\}+C_1\frac{\varepsilon_i}{k_i}P_i-C_2\rho_i\alpha_i\frac{\varepsilon_i^2}{k_i} \qquad (9)$$

Boundary Conditions

At the inlet to the duct, the following values are set for each of the four fields: 2 velocity components, density, volume fraction, k and ε. Since the quality is measured from the experiments, the inlet cv-volume fraction is set based on the quality and vapor-liquid density ratio. If a phase is not present at the inlet (α_i=0), then its inlet conditions do not affect the results, and reasonable values corresponding to zero-slip, saturated conditions are typically given. A pressure boundary condition is specified across the exit plane of the duct. No slip boundary conditions are used on the walls of the duct. Setting the system pressure and fluid type completes the flow specification.

In the three-field (cl, cv and dl) formulation used, thirteen transport equations (one continuity and two momentum equations per field; k and ε equations in the two continuous fields) and one algebraic equation (volume fraction constraint) are solved. This equals the number of unknowns (u, v, and α in each of the three fields, one pressure common to all fields, and k and ε in the cl- and cv- fields). Details of the numerical schemes are available in Siebert, *et al.* (1995).

Numerical Procedure

The system of governing differential equations is discretized using a finite volume formulation in which first order hybrid upwinding is used for the convection terms. The discretized equations are solved using the SIMPLEC algorithm [Patankar (1980)]. Pressure velocity coupling is enforced using the algorithm developed by Rhie and Chow (1983). The phase-coupling algorithm originally developed by Spalding (1980) for a non-staggered grid in the commercial code, CFDS-FLOW3D [AEA (1992)], was substantially modified to incorporate a multi-field flow scheme [Siebert and Antal (1993)]. Several different grid spacings were examined (for example, 37x16, 37x24 and 37x32) and the numerical results presented are generated with non-uniformly spaced grids (37x16) using the Cray C90 computer. This grid was found to be adequate for the experimental conditions reported. Solution convergence was measured by examining the mass, momentum and energy residuals in the continuous liquid field.

Additional measures of convergence included global mass and energy balances (typically < 10^{-5}).

Discussion of Models

Since the equations are ensemble-averaged, physical information is lost. This information is recovered in the equations through closure conditions/ models. These models represent field-to-field and field-to-wall interactions, and are underlined in Eqs. (4) and (5). The models that are categorized as drag and non-drag models are either developed here or adapted from the literature. The one-dimensional models obtained from the literature are modified to apply locally on a two-dimensional basis. The annular flow models discussed in this section are divided into two categories: 1) thin film, and 2) droplet models. The thin film contains the cl-cv interface, and are further divided into wall and interfacial models. The vapor core contains the droplets, and hence the cv-dl interface.

Thin Film Models

Wall Lateral Force

In a 3-field prediction (i.e., without the dv-field), the formation and maintenance of annular flow is determined by the forces which act on the wavy interfaces. Specifically, an aerodynamic force, called the wall lateral force, is proposed that acts on the cl-cv interface, and forces the liquid film on the wall. Antal *et al.* (1991) developed a bubbly flow lateral force to move the bubbles toward the center of the duct. In their analysis, they developed an approach to approximate the flow field interaction between a single two-dimensional circular bubble with a planar wall. The flow field is constructed using the method of images and superposition of doublet and vortex singularities. Flow circulation is introduced to ensure a no-slip boundary condition when the bubble interface touches the wall. The force on the bubble is calculated using the

Cauchy Residue Theorem. This model was modified by Kumar and Edwards (1996) using a length scale that is proportional to the hydraulic diameter instead of the bubble diameter.

The form of the annular flow wall lateral force is written as

$$M^{w} = \frac{2\alpha_{cv}\rho_{l}v_{R}^{2}}{D_{h}}\left(\left(\left(C_{w2}\frac{D_{h}}{2y_{wall_1}}\right)^{a} + (-C_{w1})^{a}\right)^{1/a} - \left(\left(C_{w2}\frac{D_{h}}{2y_{wall_2}}\right)^{a} + (-C_{w1})^{a}\right)^{1/a}\right) \tag{10}$$

where *a* is a smoothing parameter, y_{wall1} is the distance to the nearer wall, and y_{wall2} is the distance to the farther wall. The smoothing function is used to remove a discontinuity in the wall force. For this analysis, following an optimization study on the coefficients, values of -1.7×10^{-5} and 2×10^{-5} are used for C_{w1} and C_{w2}. Although no 'separate effects' experiment was performed in annular flow to justify this model, this lateral force has been found to be important to maintain the liquid film on the wall, as seen later in the Results section.

Wall Shear

It is assumed that the continuous liquid is in contact with the wall in annular flow, and flows as single-phase Couette flow along the wall. Therefore, the wall shear is applied only to the cl-field and not to the dl- or cv-fields. Wall shear stress is related to the turbulence kinetic energy by

$$\tau_{w} = C_{\mu}^{0.5}\rho_{l}k_{p,\,cl}\,. \tag{11}$$

Using the definition of friction velocity and the relationship in Eq. (11), the scaled variable, y^{+}, can be redefined as

$$y^{+} = \frac{\rho_{l}(y_{c})C_{\mu}^{0.25}k_{p,\,cl}^{0.5}}{\mu_{l}} \tag{12}$$

where y_c is half the thickness of the film, given by the product of the cl-volume fraction and the nodal distance, y_p. Now, the wall shear stress can be written as

$$\tau_w = T_m u_{p,cl}, \text{ where} \tag{13}$$

$$T_m = \frac{\rho_l C_\mu^{0.25} k_{p,cl}^{0.5}}{u_p^+}. \tag{14}$$

The non-dimensional velocity, u_p^+, uses a law-of-the-wall formulation which is recast as

$$u_p^+ = \frac{1}{\kappa}\ln(Ey^+) \tag{15}$$

where E and κ are new constants to be determined for two-phase flows. Eqs. (13), (14), and (15) provide the wall shear stress at every wall node in the streamwise direction in terms of the neighboring node p perpendicular to the wall. C_μ in Eq. (14) takes a constant value of 0.09. The constants E and κ in Eq. (15) are the single-phase values, 9.0 and 0.4, respectively.

Interfacial Shear

Interfacial shear models have been developed in the literature for annular flow based on the extensions of single-phase flow approaches to account for the wavy interface and entrainment. By considering that the waves on the interface act as roughness elements, a two-phase friction factor similar to the pipe friction factor for single-phase flow has been developed. The liquid film is treated as a rough surface and can be expressed in terms of an equivalent sand roughness. Gill *et al.* (1963) calculated the equivalent sand roughness from the pressure drop and gas Reynolds number in air-water flows using a single-phase friction factor chart. The roughness height varies quadratically with the film thickness and is approximately independent of the film flow rate. Although this deduction was made with limited data, the data showed at least qualitatively that the interfacial shear increased with increasing film thickness.

Wallis (1969) showed that at atmospheric pressure for air-water flows, a wavy annular film is equivalent to a sand roughness of four times the film thickness over the range $0.001 < k_s/D < 0.03$, where k_s is the grain size of the equivalent sand roughness. He stated that the interfacial shear stress depends on the difference between the gas velocity and some characteristic interface velocity. For gas velocity much larger than liquid velocity, he proposed an interfacial shear model as:

$$\tau_i = f_i \frac{1}{2} \rho_g u_g^2 \tag{16}$$

where

$$f_i = f_{sp}\left(1 + 300\frac{\delta}{d_h}\right), \tag{17}$$

δ is the film thickness, and f_{sp} is the single-phase friction factor taken to be 0.005. The quantity in parenthesis in Eq. (17) is the two-phase correction factor, which is merely a simplification of the shift in the logarithmic laws proposed in the literature [Dobran (1983), Hewitt (1991) and Kumar and Edwards (1996)].

cl-cv interfacial area density

In order to model the cv-cl interfacial area density, some assumptions about the interface must be made. For this analysis, the continuous liquid is assumed to flow as a film along the wall. The wall is assumed to be completely wetted ($\alpha_{cl} = 1.0$ at the wall), and the cl-volume fraction decreases rapidly in the first few nodes away from the wall. In the actual flow situation, the steepness of the transition from the wall ($\alpha_{cl} = 1$ to the core α_{cl}~0) is determined by the film thickness and wave characteristics of the interface. These wave characteristics, in turn, are determined by the flow rates, heat fluxes, and momentum forces acting on the interface. The smooth transition in α_{cl} may be interpreted as the effect of a wavy interface on the mean void distribution, although the details of the wave structure are not captured by this model.

For smooth films flowing parallel to the walls, the interfacial area density can be calculated from the gradient normal to the wall in the cl void fraction, or

$$A'''_{cl-cv} = \nabla\alpha \cdot \hat{n} \tag{18}$$

where $\hat{n}$ is a vector normal to the wall.

Droplet Models

Droplet Entrainment

The total entrainment rate is modeled as the sum of two separate physical phenomena: the entrainment of droplets from the roll wave shearing and the break-up of continuous liquid bridges, as

$$\Gamma_{cl-dl} = \Gamma^{f}_{cl-dl} + \Gamma^{b}_{cl-dl}. \tag{19}$$

It is assumed that these two types of entrainment are separable and occur in different regions of the flow. The film entrainment model of Kataoka and Ishii (1983) was adapted to multidimensional predictions by extending the original averaged one-dimensional models to two dimensions. It is assumed that the entrainment mass flux given by the Kataoka and Ishii (1983) correlation is the same for a film in a small thickness/width duct whose surface area and thickness is the same as that in the cylindrical geometry. It is further assumed that the correlation can be "localized" by replacing the cross section-averaged quantities in the dimensionless numbers with local values. The entrainment rate, Γ^{f}_{cl-dl}, is given by the following set of equations.

$$\frac{G_E D_h}{\mu_{cl}} = 6.6\mathrm{x}10^{-7} \mathrm{Re}_l^{0.74} \mathrm{Re}_{cl}^{0.185} \mathrm{We}^{0.925} \left(\frac{\mu_g}{\mu_f}\right)^{0.26}, \text{ where} \tag{20}$$

$$\mathrm{Re}_l = \frac{\rho_l(\alpha_{dl}u_{dl} + \alpha_{cl}u_{cl})D_h}{\mu_l}, \tag{21}$$

$$\mathrm{Re}_{cl} = \frac{\rho_l \alpha_{cl} u_{cl} D_h}{\mu_l}, \text{ and} \tag{22}$$

$$We = \frac{\rho_v(\alpha_{cv}u_{cv})^2 D_h}{\sigma}\left(\frac{\rho_l-\rho_g}{\rho_g}\right)^{1/3}. \tag{23}$$

The local mass flux is then calculated and applied through the local cl-cv interfacial area density, as

$$\Gamma^f_{cl-dl} = G_E A'''_{cl-cv}. \tag{24}$$

The droplets are also formed in the transition regime where the liquid bridges break up. The fragmentation is caused by flow instabilities and surface tension. These droplets have varying size. A triangular relationship based on the concept of a critical Weber number, breakup time and velocity history by Pilch and Erdman (1987) is used in this model. When the breakup occurs, the droplet velocity is assumed to be equal to the mean velocity of the cl-field from which it was created. The mass transfer rate due to breakup is given by the following set of equations.

$$\Gamma^b_{cl-dl} = C_1\overline{\alpha_{cv}}\rho_l\ f\ \alpha_{cl}, \text{ where} \tag{25}$$

$$f = Fu_{cv}\sqrt{\rho_v/\rho_l}/D_o\ , \tag{26}$$

$$D_o = 2\sqrt{\frac{\sigma}{g(\rho_l-\rho_g)}}\text{ , and} \tag{27}$$

$$F = 0.07(We^{0.5}-5.0). \tag{28}$$

Eq. (28) is a simplified correlation developed here from Pilch and Erdman's (1987) measurements for different Weber number ranges. Pilch and Erdman (1987) proposed their correlation for the breakup of isolated liquid drops that are suddenly exposed to a high-velocity field. Weber number, We, in Eq. (28) is given by

$$We = D_o\rho_v u_{cv}^2/\sigma \tag{29}$$

In the current flow situation, as can be noted in Eq. (25), liquid breakup of the cl-field occurs only when the cv-field is present, i.e., in the presence of an interface. Therefore, it may be viewed that the cl-field present in the node along with the cv-field is a large drop which is about to break up.

Droplet Deposition

The deposition model is a simple, flux based model that approximates the mass flow rate of droplets into the continuous liquid film as

$$\Gamma_{dl-cl} = \rho_l u_{dl} A''' \quad . \tag{30}$$

The droplet velocity is given by the speed at which dl is carried normal to the plane of deposition.

Drop Size

Several correlations for mean drop size are available in the literature [Tatterson *et al.* (1977), Ueda (1979) and Kocamustafaogullari *et al.* (1994)]. Ueda's correlation is chosen for this study because it is based on drop size data taken for the refrigerant fluid R-113, which has a lower surface tension and low vapor-to-liquid density ratio as compared to air-water flows. Comparisons of Ueda's correlation with the measured average drop size are presented in Part I of this paper [Trabold and Kumar (1998)]. The correlation is given by

$$d_D = 5.8 \times 10^{-3} D_h \left[\frac{\sigma}{\mu_v u_{cv}} \left(\frac{\rho_g}{\rho_l} \right)^{1.25} \right]^{0.34} \quad . \tag{31}$$

Droplet Drag

This model, initially proposed by Ishii and Zuber (1979), was developed for the viscous and the distorted particle regime from similarity criteria derived between single and multiple particle behavior and the definition of a mixture viscosity, as

$$C_D = \max \left(\begin{array}{l} \frac{24}{Re_D}(1.0 + 0.1 Re_D^{3/4}) \\ \frac{2}{3} d_D \left[\frac{g \Delta\rho}{\sigma} \right]^{1/2} \quad \left[\frac{1 + 17.67(1-\alpha_{dl})^{18/7}}{18.67(1-\alpha_{dl})^3} \right]^2 \end{array} \right) \text{, where} \tag{32}$$

$$Re_D = \frac{\rho_g |\underline{v}_r| d_D (1-\alpha_D)^{2.5}}{\mu_g} . \qquad (33)$$

The factor, $(1-\alpha_D)^{2.5}$ modifies the viscosity and thus accounts for the increased drag on a non-spherical droplet. This factor also accounts for the effect of the interaction of multiple droplets on each other.

Droplet Lift

A non-drag force which plays a role in the annular vapor core is the lift force which appears as a source term in the momentum equation.The constitutive relationship given in Eq. (34) models the force generated as an inviscid fluid with constant strain and rotation flows past a sphere. This force captures the influence of the continuous field velocity gradient on the dispersed field, thereby impacting the transverse distribution of the dispersed phase. It is based on the derivation for a bubbly lift force using a non-inertial reference frame which rotates at a rate equal to the far field fluid rotation [Drew and Lahey (1987)]. Potential flow theory is used to construct the inviscid flow field around the sphere and the force is calculated by integrating the interfacial pressure over the sphere's surface. In the droplet field, the fields are switched, and the lift force is given by

$$M^L_{cv} = -M^L_{dl} = C_L \rho_{cv} \alpha_{dl} \underline{v}_R \times (\nabla \times \underline{v}_{cv}), \qquad (34)$$

where

$$\underline{v}_R = \underline{v}_{cv} - \underline{v}_{dl} . \qquad (35)$$

The lift coefficient, C_L, for a single bubble is 0.5 for inviscid flows, but may be much lower for highly viscous flows [Eichhorn and Small (1964)]. In this study, C_L is taken to be 0.2.

Turbulent Dispersion of Droplets

A turbulent dispersion model for bubbles was developed by de Bertodano (1992) by making an analogy of thermal diffusion of air molecules in the atmosphere. A thought experiment was made for a bounded turbulent bubbly mixture whose dispersion is similar to that of air molecules, except that the motion of the bubbles is produced by the turbulent energy of the liquid phase instead of the thermal energy of the air molecules. In annular flow, the dispersion model is adapted for liquid droplets in a vapor medium, and is given by

$$T_{dl}^{d} = -0.1\rho_v k_{cv} \nabla \ln \alpha_{dl}. \tag{36}$$

Since this model involves a gradient of void fraction, it is possible to construct it from the cross-correlation term of fluctuating void fraction and fluctuating velocity.

cv-dl Interfacial Area Density

The droplet interface is assumed to arise around a spherically shaped dispersed field (dl) whose diameter is locally defined (see the 'Drop Size' section). Based on the spherical equivalent drop size, the interfacial area density is given by

$$A'''_{cv-dl} = \frac{6\alpha_{dl}}{d_D}. \tag{37}$$

Results of Integrated Model Predictions and Comparisons

The models described in the previous section have been implemented into the three-field, two-dimensional solver, and the results are compared with adiabatic annular flow data obtained in refrigerant (R-134A) flows in a vertical duct with a cross-section aspect ratio of 22.5 in Part I of this paper [Trabold and Kumar (1998)]. It was shown in the modeling section that the mechanisms controlling droplet formation, dispersion of these droplets in the vapor core, deposition of the droplets and the continuous liquid on the wall, forces acting on these droplets, and the thin film are important for model development. Wherever possible, these individual models were compared with available data. In this section, an integrated model prediction is performed to test these models. Averaged void fraction data and droplet velocity were obtained using a gamma densitometer and a hot film anemometer, respectively. Table 1 provides the flow conditions for which the computational results were obtained.

Comparison of 1-D vs. 2-D Results

For proper adaptation of one-dimensional models in the literature in a two-dimensional analysis code, appropriate model coefficients must be determined. For example, interfacial shear given by Eqs. (16) and (17) was originally formulated for flow in a circular tube where the interfacial area is the equivalent of that for a film of thickness δ on the walls. The continuous liquid layer extends from the wall to the wave troughs, and the disturbed wavy layer of thickness from the crests to the troughs of the waves. Due to this distortion of the interface by the waves of small and large amplitudes (sketch shown in figure 1), it is difficult to define δ. Further, it is inappropriate to use such a parameter in a local formulation. When interfacial shear is applied on a local basis, it must be modified to account for the effect of averaging on the model. This is done by determining the local interfacial shear at every node by replacing δ with y in Eq. (17), and applying it to a local interfacial area. This ensures that when the local interfacial area density is zero, the interfacial shear is also zero.

The magnitude of the interfacial shear depends on the local relative velocity; therefore, in Eq. (16), u_g is replaced by $(u_{cv} - u_{cl})$ as was originally intended by Wallis (1969). Since, this local velocity difference is much smaller than the difference in the average velocities, an empirical coefficient of 1.34 was obtained by matching the void fraction data. Using this parameter, two-dimensional predictions were obtained for different mass flux and a void fraction of 90%. The interfacial shear was then averaged across the test section and compared with the equivalent one-dimensional interfacial shear as shown in Figure 2. It can be seen from this figure that the distribution coefficient captures the effects of averaging adequately at low flows. At the highest mass flux, the two-dimensional prediction is about 15% lower than to its one-dimensional counterpart. This means that the coefficient is probably dependent on a global parameter such as Reynolds number. Since the overall predictions appeared to be good, no correction to the distribution coefficient was made.

The contour plots in figure 3a shows the axial development of the phasic volume fractions in the test section. The three color contour plots show the volume fraction in a x-y slice plane for the continuous liquid, dispersed liquid, and continuous liquid fields, respectively. Figure 3b shows the axial variation of the transverse average volume fraction for each field. The flow is induced by setting an inlet cv-volume fraction based on the inlet quality measured from the experiments, x_i, using the relationship,

$$\alpha_{cv} = \frac{1}{1+\frac{\rho_v}{\rho_l}\left(\frac{1-x_i}{x_i}\right)} . \tag{38}$$

The annular flow structure forms very rapidly, and a thin liquid film develops at the walls and reaches a fully developed condition within the first few hydraulic diameters in the streamwise direction. Film entrainment dominates in the annular region, with the local entrainment rate, Γ^{f}_{cl-dl}, peaking at the location of the film interface. The shift of mass from cl to dl due to bridge break-up, Γ^{b}_{cl-dl}, dominates near the inlet where the flow enters as a mixture of continuous liquid and continuous vapor. Here, bridges of liquid between the vapor pockets are fragmented into dispersed liquid. After the flow develops, the cross-section average void fraction prediction is compared with experimentally measured void fraction at two different downstream locations (Figure 3b). This crosscheck was done for every run and the comparisons were found to be good.

In Figures 4 through 11, local comparisons of droplet velocity and the void fraction are made for 8 cases at two system pressures, different flow rates and void fractions at or above 80%. These flow conditions are provided in Table 1, with the first three cases run at 1.4 MPa and the next five at 2.4 MPa. For all these cases, the modeling coefficients provided in the previous section remained the same. High void fraction flows are chosen such that the flow is predominantly two-dimensional for valid comparison with analysis. In general, the local predictions of void fraction and droplet velocity are remarkably good, validating the overall modeling approach taken. Specific observations of general model behavior, deviations and discrepancies in Figures 4 to 11 are discussed below.

In Figure 4 , for 1.4 MPa, the liquid film on the wall is thick at α=0.8, and the flow is locally annular is the vapor core. The void profile maintains a center-peaked distribution as the flow appears to undergo late stages of transition. A mixture of continuous vapor slugs separated by liquid bridges flow together in a continuous liquid field. The fully annular void prediction is flatter due to fairly uniformly distributed liquid droplets in the vapor core. The droplet volume fraction prediction for this case is 18%. The model does not discriminate between the droplets and liquid ligaments as it considers them as one distributed liquid (dl) field, and therefore, it is not surprising that for this case which is not purely annular, there is a very high dl-volume fraction in the vapor core.

As the average void fraction is increased to 95% at 1.4 MPa (Figures 5 and 6), the gas core velocity increases and tears the liquid droplets from the surface of the thin film. The liquid film becomes thinner, and a noticeable wall-peaked distribution in void fraction occurs. The dip in void fraction at the centerline is probably due to the migration of droplets from the edges of the test section where high amplitude roll waves are formed. Since the film is thicker near the edges than at the flat walls, the fragmentation of the edge films gives rise to much bigger droplet diameters. This three-dimensionality in the flow field due to a finite aspect ratio of 22.5 is not captured by the current two-dimensional predictions. For these high flows, the drop size measurement profiles display an increasing trend towards the centerline from the wall (Trabold and Kumar, 1998). The drop size model provided in the previous section is based on the premise that the drop size is controlled by the interaction between the dl and the cv fields. Therefore, the droplets entrained near the liquid film, as predicted by the model, tend to be larger in size compared to those in the main vapor core where the droplets are subjected to turbulent break up. Thus, the current model cannot predict the increasing trend in the drop size measurements. The predicted drop size profiles (not shown here) always have a decreasing trend, but the average predicted value was found to be close to the average experimental value.

The entrainment rate as given by the droplet entrainment model is enhanced at the higher pressure of 2.4 MPa for which the gas density is higher and the surface tension is lower. In general, at very high void fractions (α>0.9), the liquid film is relatively thin around the perimeter of the duct. The droplets emanating from the edge films are similar in size compared to other entrained droplets, and the two-dimensional approximation is reasonable for numerical analysis. Three-dimensional formulation is necessary to predict lower void fraction annular flows. Since the liquid-to-gas density ratio for 2.4 MPa is 7.3 (closely simulating steam-water conditions at very high pressures) which is nearly half of that for 1.4 MPa, the droplet velocities for 2.4 MPa are lower than their lower pressure counterparts (Figures 7-11). These velocities range from ~1 m/sec to ~10 m/sec, and are closer to the corresponding mixture velocities for these flows. Droplet velocities reported in the literature for annular flows are in two-phase annular flows with very low vapor-to-liquid density ratios (as in air-water), and are an order of magnitude higher than the current velocities.

Summary and Conclusions

A three-field model capable of predicting both local and global annular flow characteristics has been developed. Locally based droplet and film models have been either developed here or adapted from the literature for closure of the governing equations. Interfield (liquid-liquid) models, interphase (liquid-vapor) models and other force models are locally applied to appropriately separate the liquid film from the vapor core, and to capture the physics of the droplet motion. This paper provides substantial information on the individual and integrated effects of these models in annular flow, and compares the predictions with the average and local void fraction and droplet velocities in a refrigerant fluid (R-134a) using hot film anemometry and gamma densitometry.

The proposed set of models appears to adequately predict local distribution of the variables in purely annular flows. However, the model set needs to be strengthened for the prediction of slug-to-annular transition flows at void fractions in the range of 70% to 85%. In this regard, including a fourth dispersed vapor field to account for the trapping of bubbles in the liquid film, and a three-dimensional analysis may be necessary. As a consequence of the interfacial waves breaking at the tips, droplet deposition and droplet entrainment processes have a significant impact on the interrfacial shear stress. The current models for drop size and entrainment/deposition need to be reevaluated and their effect on the current interfacial shear model tested. Additional data on the interfacial wave frequency, velocity and area concentration obtained in Part I of this paper (Trabold and Kumar, 1998) should be used to develop mechanistic interfacial shear model that can be locally applied.

Acknowledgements: The authors are grateful to Dr. D.P. Edwards for his initial model development efforts and many fruitful discussions, and to Mr. B.W. Siebert and Dr. R.F. Kunz for their efforts in code development.

References

Antal, S.P, Lahey, R.T., Jr. and Flaherty, J.E. (1991) "Analysis of Phase Distribution in Fully Developed Laminar Bubbly Two-Phase FLow," *Int. J. Multiphase Flow*," Vol. 17, No.5, pp. 635.

Azzopardi, B.J. and Teixeira, J.C.F. (1994) "Detailed Measurements of Vertical Annular Two-Phase Flow - Part I: Drop Velocities and Sizes," *ASME J. Fluids Eng.*, Vol 116, pp. 792-795.

Cousins, L.B. and Hewitt, G.F. (1968) "Liquid Phase Mass Transfer in Annular Two-Phase Flow: Droplet Deposition and Liquid Entrainment," UKAEA Report AERE-R5657.

Dobran, F. (1983) "Hydrodynamic and Heat Transfer Analysis of Two-Phase Annular Flow with a New Liquid Film Model of Turbulence," *Int. J. Heat Mass Transfer*, Vol. 26, No. 8, pp. 1159-1171.

Drew, D.A. and Lahey, R.T. (1987) "The virtual mass and lift force on a sphere in rotating and straining inviscid flow," *Int. J. Multiphase Flow*, Vol. 13(1), pp. 113-121.

Drew, D.A. (1992), "Analytical modeling of multiphase flows,"*Boiling Heat Transfer*, R.T. Lahey, editor. Elsevier, pp.31-84.

Eichhorn, R. and Small, S. (1964) "Experiments on the lift and drag of spheres suspended in a poiseuille flow," *J. Fluid Mech.* **20**(3), 513.

FLOW3D (1992) "Release 3.2 User's Manual Computational Fluid Dynamics Services," *AEA Industrial Technology*, Harwell Laboratory, Oxford, UK.

Gill, L.E., Hewitt, G.F., Hitchon, J.W. and Lacey, P.M.C. (1963) "Sampling Probe Studies of the Gas Core in Annular Two-Phase Flow-I: The Effect of Length on Phase and Velocity Distribution," *Chem. Eng. Sci.*, Vol. 18, pp. 525-535.

Hall Taylor, N.S., Hewitt, G.F. and Lacey, P.M.C. (1963) "The Motion and Frequency of Large Disturbance Waves in Annular Two-Phase Flow of Air-Water Mixtures," *Chem. Engng. Sci.*, Vol. 18, pp. 537-552.

Hewitt, G.F. and Hall-Taylor, N.S. (1970) *Annular Two-Phase Flow*, Pergamon Press.

Hewitt, G.F. and Govan, A.H. (1990) "Phenomena and Prediction in Annular Two-Phase Flow," ASME FED-Vol. 99, Advances in Gas-Liquid Flows, J.H. Kim *et al.* (eds.).

Hewitt, G.F. (1991) "Annular Flow Phenomena," *Proc. Japan Soc. Multiphase Flow on Waves and Turbulence in Multiphase Flow, and its Application*, September, pp. 126-154.

Ishii, M. and Zuber, N. (1979) "Drag Coefficient and Relative Velocity in Bubbly, Droplet or

Particulate Flow," *AIChE J.*, Vol. 25, 843-855.

Kang, H.C. and Kim, M.H. (1993) "The Relation Between the Interfacial Shear Stress and the Wave Motion in a Stratified Flows," *Int. J. Multiphase Flow*, Vol. 19, No.2, pp. 35-49.

Kataoka, I., Ishii, M. and Mishima, K. (1983) "Generation and Size Distribution of Droplet in Annular Two-Phase Flow," *ASME J. Fluids Eng.*, Vol. 105, pp. 230-238.

Kataoka, I. and Ishii, M. (1983) "Entrainment and Deposition Rates of Droplets in Annular Two-Phase Flow," ASME-JSME Thermal Engineering Joint Conference, Vol. 1, pp 69-80.

Kocamustafaogullari, G., Smits, S.R. and Razi, J. (1994) "Maximum and Mean Droplet Sizes in Annular Two-Phase Flow," *Int. J. Heat Mass Transfer*, Vol. 37, pp. 955-965.

Kumar, R. and Edwards, D.P. (1996) "Interfacial Shear Modeling in Two-Phase Annular Flow," Proc. ASME Heat Transfer Division, Intl. Mech. Eng. Congress and Exposition, Atlanta, GA, HTD-Vol. 334, pp. 381-389.

Lopez de Bertodano, M. (1992) "Turbulent bubbly two phase flow in a triangular duct," Ph.D. Thesis, Rensselaer Polytechnic Institute, Troy NY, 1992.

Patankar, S.V. (1980) "*Numerical Heat Transfer and Fluid Flow*," Hemisphere Publishing Inc. NY.

Pilch, M. and Erdman, C.A. (1987) "Use of Breakup Time Data and Velocity History Data to Predict the Maximum Size of Stable Fragments for Acceleration-Induced Breakup of a Liquid Drop," *Int. J. Multiphase Flow*, Vol. 13, No. 6, pp 741-757.

Rhie, C.M. and Chow, W.L. (1983) "Numerical study of the turbulent flow past an airfoil with trailing edge separation," *AIAA J.*, Vol. 21(11), 1525-1532.

Siebert, B.W. and Antal, S.P. (1993) "An IPSA-based two-fluid algorithm for boiling multi-phase flows," *First CFDS Int. User Conf.* Oxford, UK.

Siebert, B.W., Maneri, C.G., Kunz, R.F. and Edwards, D.P. (1995) A four-field model and CFD implementation for multi-dimensional, heated two-phase flows. *Proc. of the 2nd Int. Conf. on Multiphase Flow*, Kyoto, Japan.

Spalding, D.B. (1980) "Mathematical methods in nuclear reactor thermal-hydraulics," *Proceeding of ANS Meeting on Nuclear reactor Thermal-Hydraulics*, R. T. Lahey, ed., pp. 1979-2023.

Tatterson, D.C., Dallman, J.C. and Hanratty, T.J. (1977) "Drop Sizes in Annular Gas-Liquid Flows." *AIChE J.*, Vol. 23, pp. 68-76.

Trabold, T.A. and Kumar, R. (1998) "High Pressure Annular Two-Phase Flow in a Narrow Duct - Part I: Local Measurements in the Droplet Field," submitted to *J. Fluids Eng*.

Ueda, T. (1979) "Entrainment Rate and Size of Entrained Droplets in Annular Two-Phase Flow," *Bull. JSME*, Vol. 22, pp.1258-1265.

Wallis, G.B. (1969), *One-dimensional Two-Phase Flow, McGraw-Hill*, New York.

Case No.	System Pressure MPa	Flow Rate kg/hr	Average Void Fraction	Inlet Quality	Density Ratio ρ_l/ρ_g
1	1.4	532	.80	.24	16.2
2	1.4	532	.95	.48	16.2
3	1.4	1064	.95	.42	16.2
4	2.4	106	.94	.92	7.3
5	2.4	106	.90	.79	7.3
6	2.4	266	.92	.66	7.3
7	2.4	532	.94	.70	7.3
8	2.4	1064	.90	.49	7.3

Table 1: Flow Conditions used for model validation

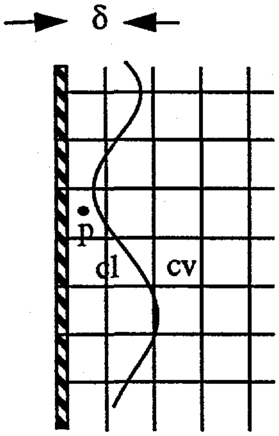

Figure 1: Schematic of the computational grid across the interface

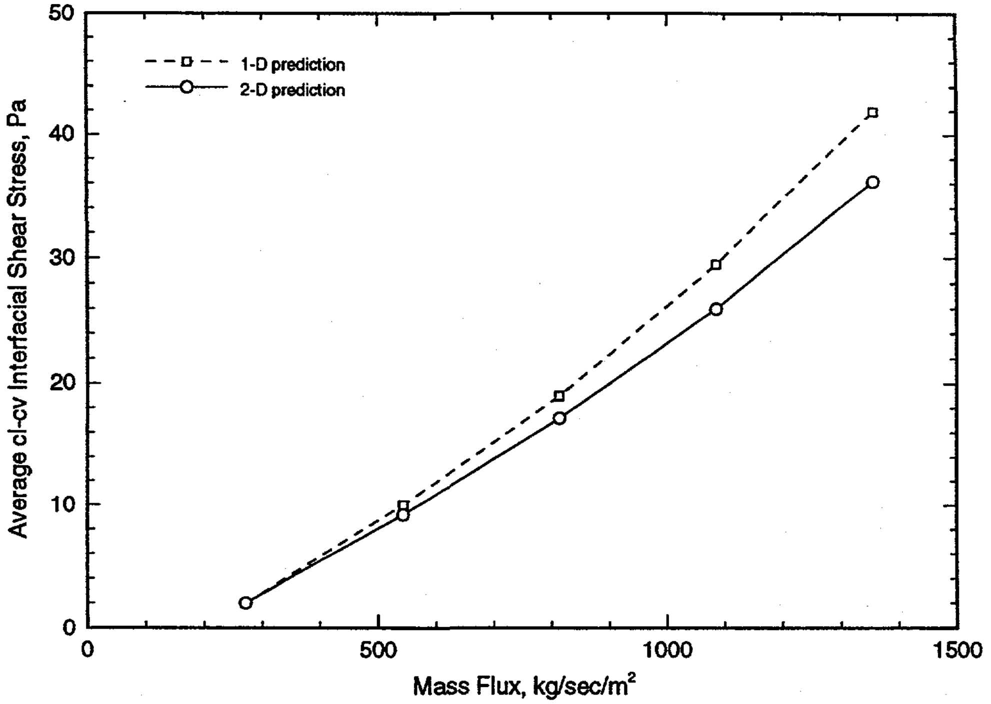

Figure 2: Comparison of Average Interfacial Shear Stress Between One-Dimensional and Two-Dimensional Analysis

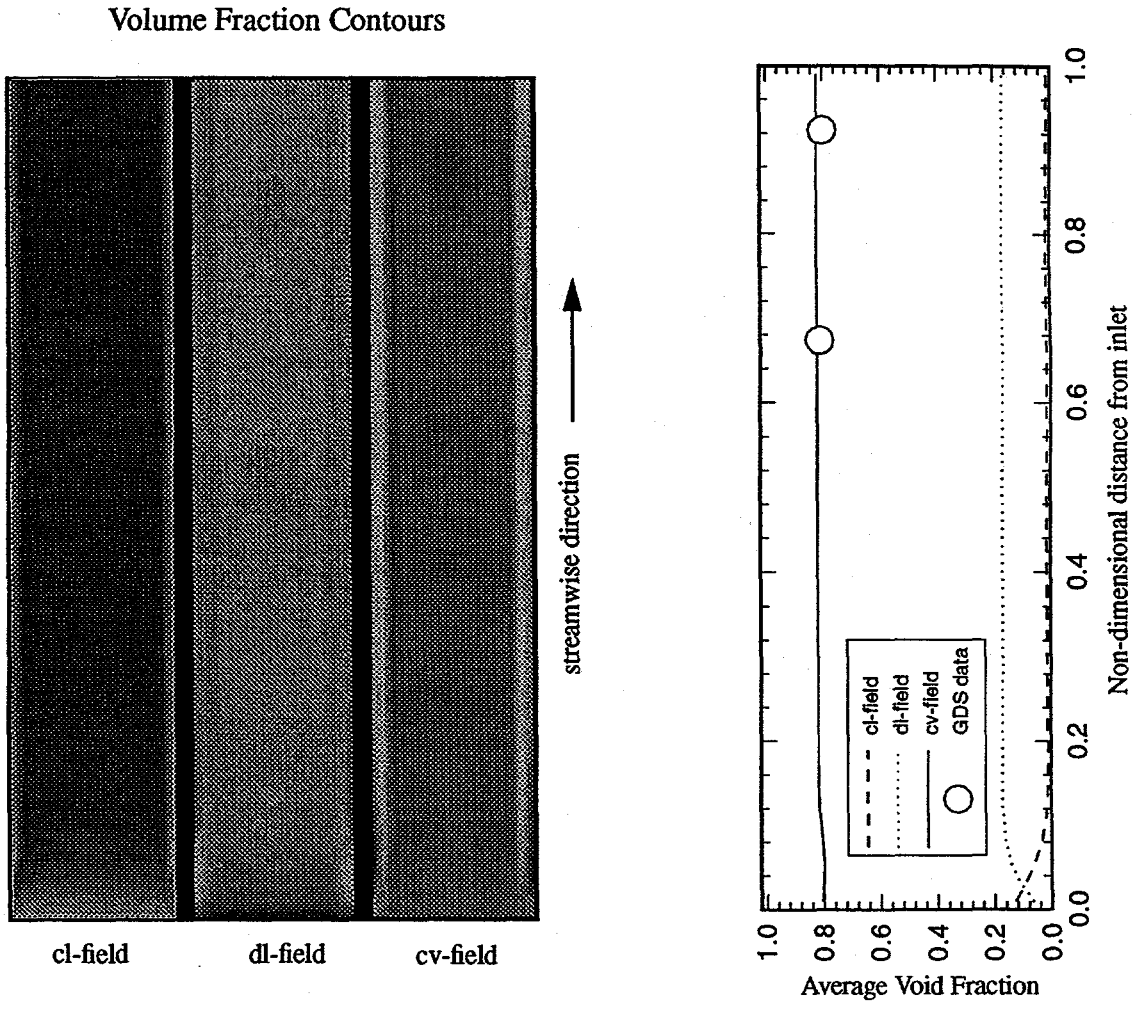

(a) (b)

Figure 3: a) Contour plots of volume fraction in each field; b) Corresponding average volume fraction profiles along the streamwise direction and comparison with GDS data

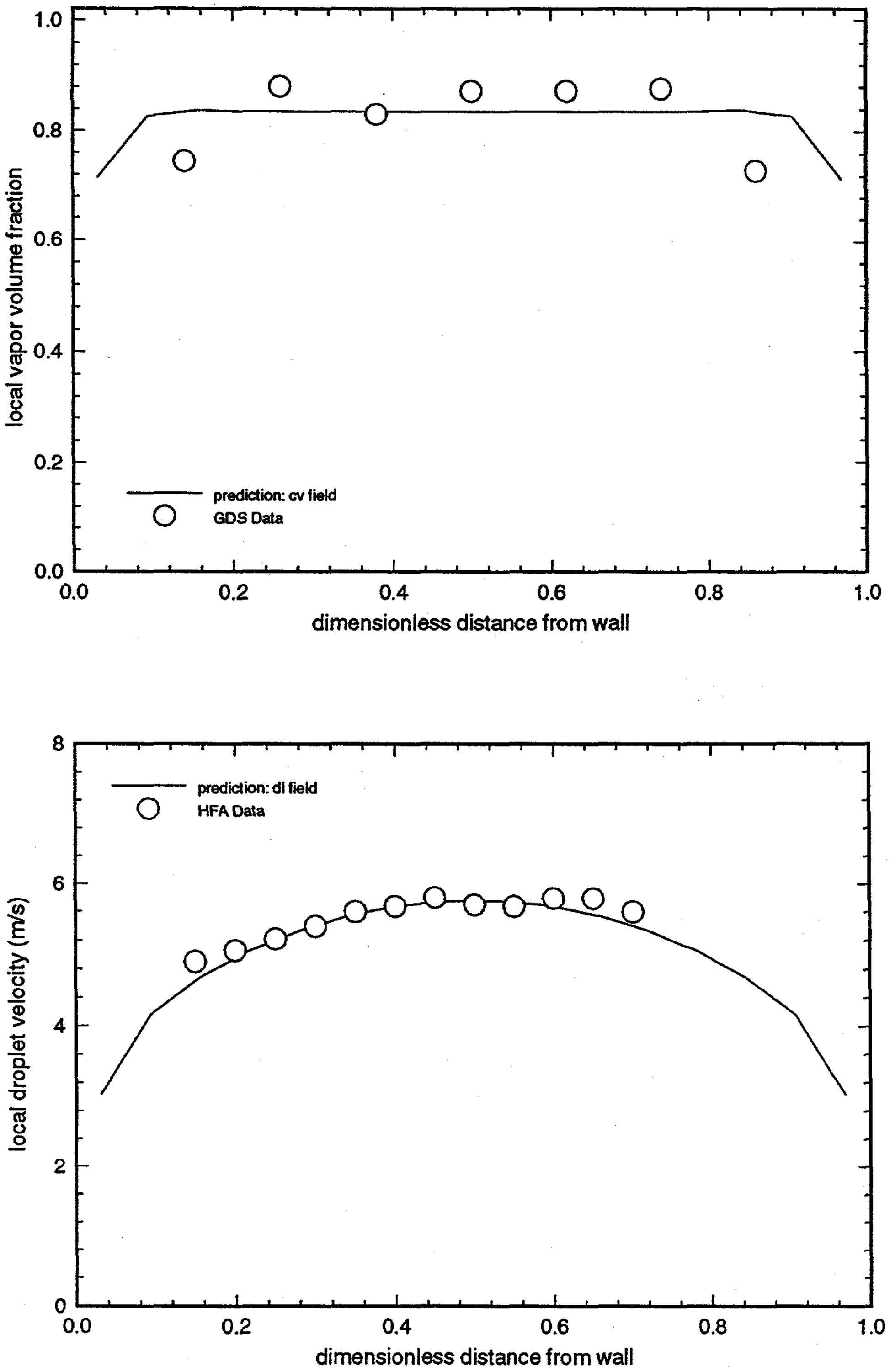

Figure 4: Comparison of Model Predictions with Experiments.

Case 1: P=1.4 MPa; w=532 kg/hr; $\bar{\alpha}$=0.8

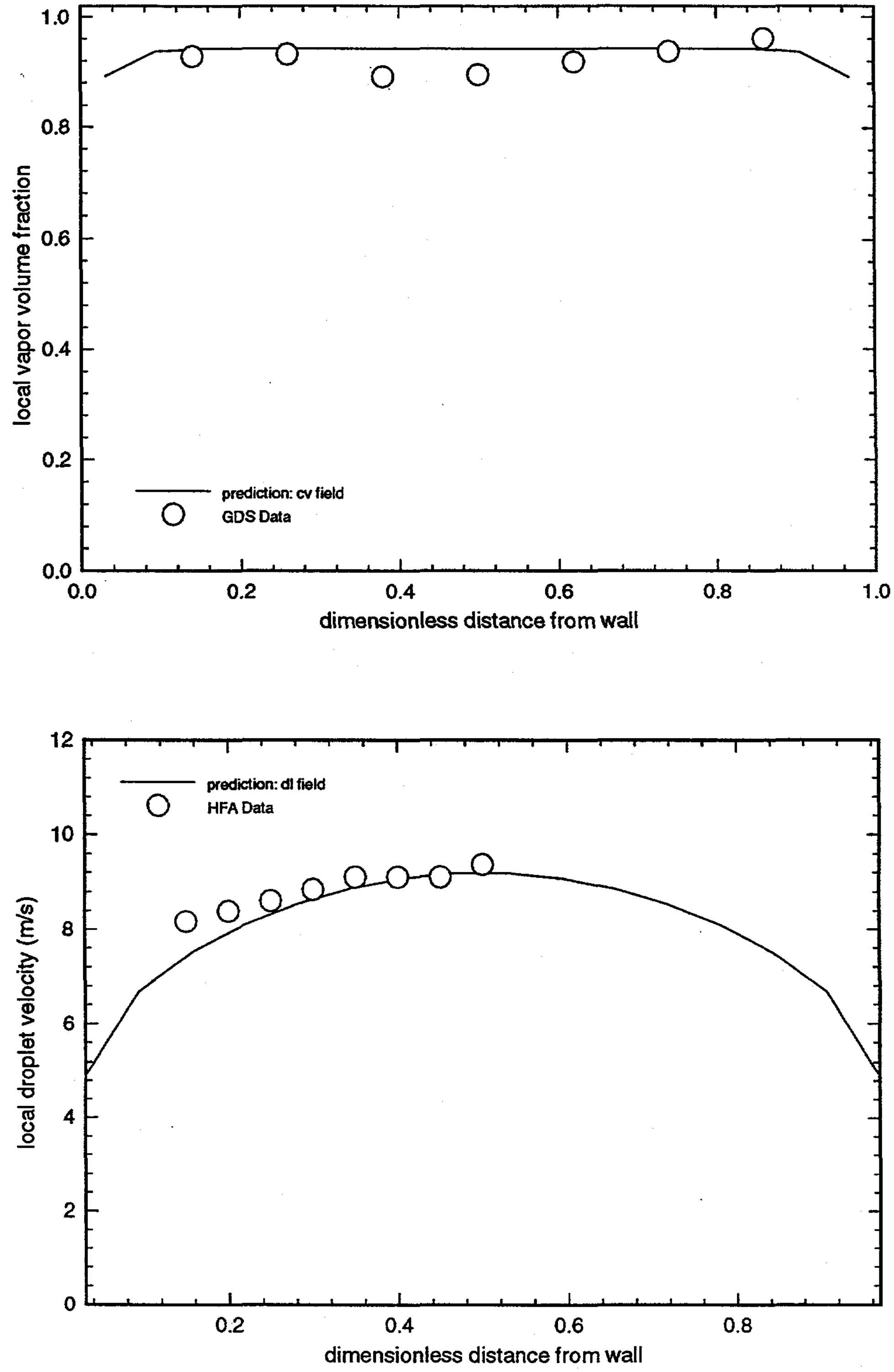

Figure 5: Comparison of Model Predictions with Experiments.

Case 2: P=1.4 MPa; w=532 kg/hr; $\overline{\alpha}$=0.95

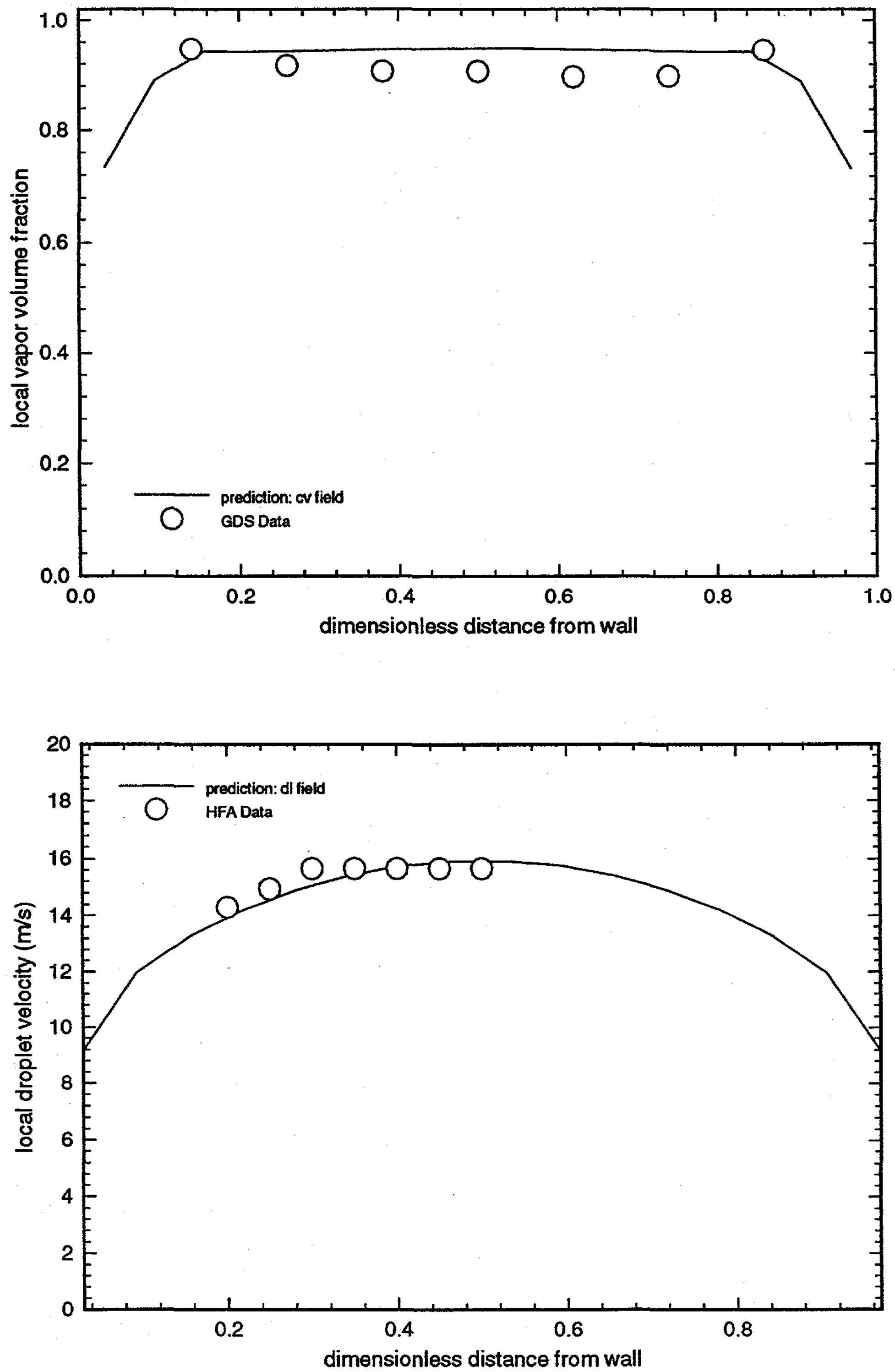

Figure 6: Comparison of Model Predictions with Experiments.

Case 3: P=1.4 MPa; w=1064 kg/hr; $\bar{\alpha}$=0.95

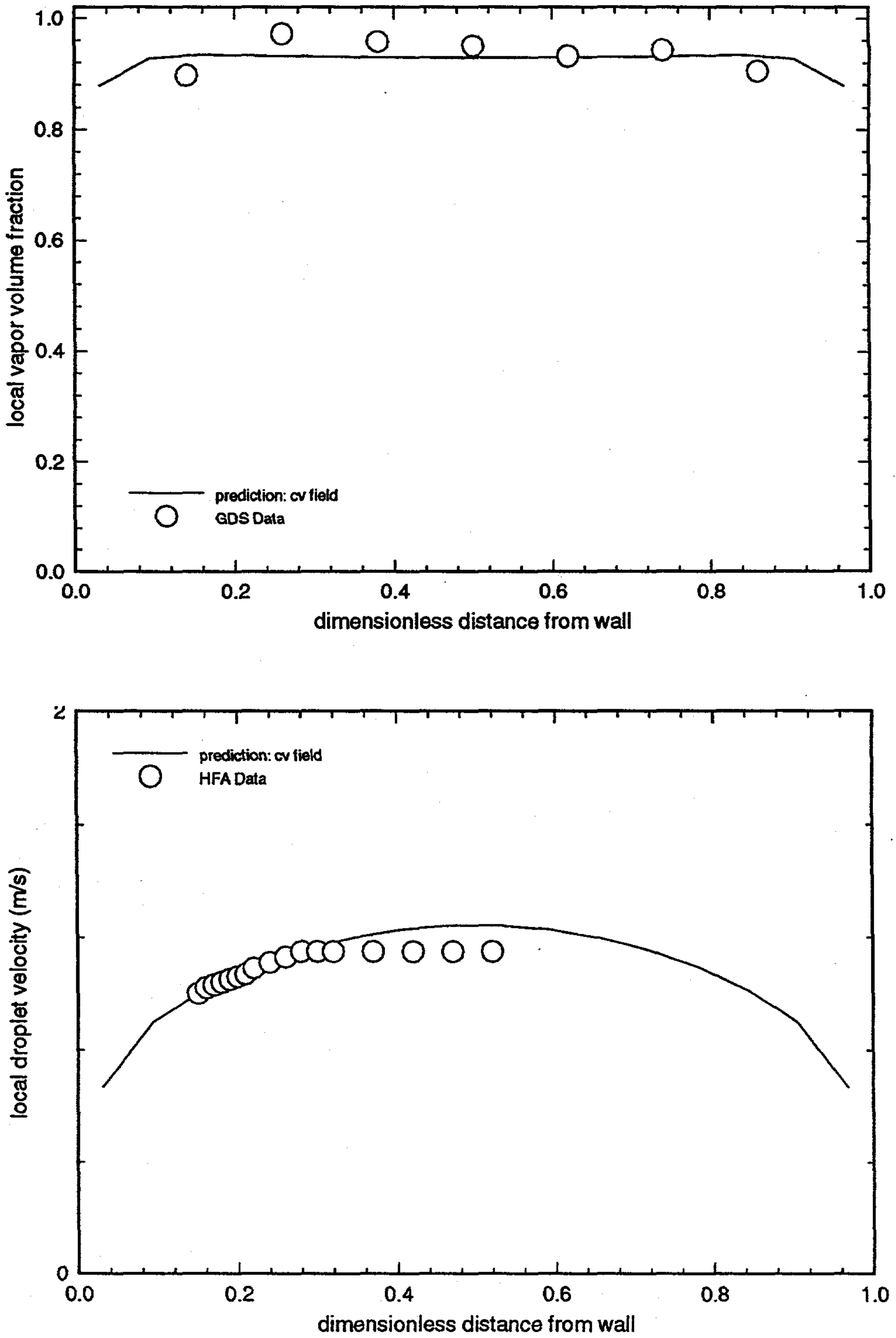

Figure 7: Comparison of Model Predictions with Experiments.

Case 4: P=2.4 MPa; w=106 kg/hr; $\bar{\alpha}$=0.94

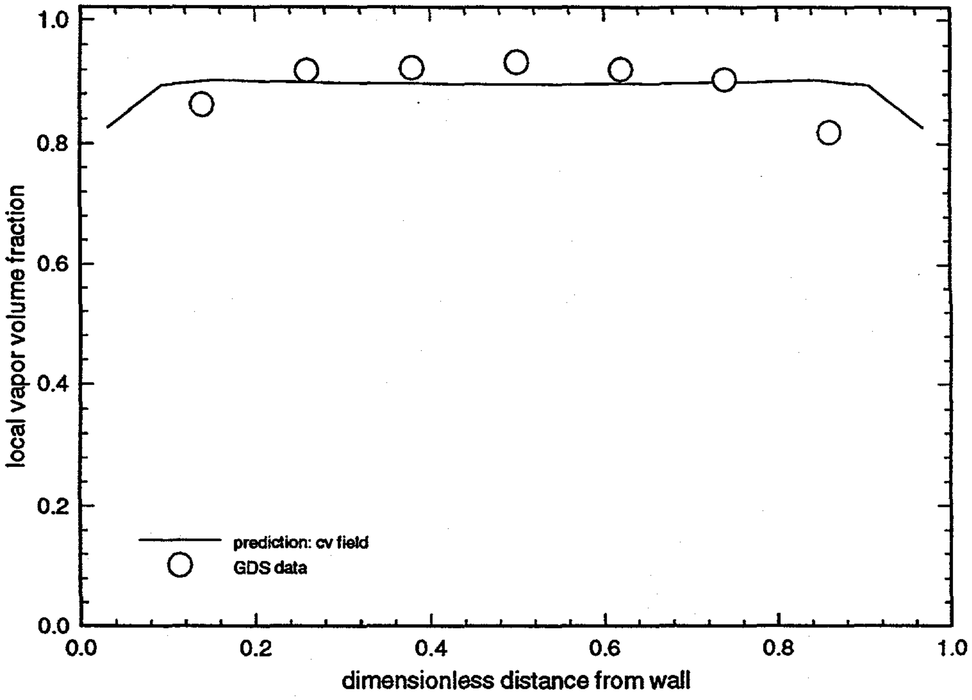

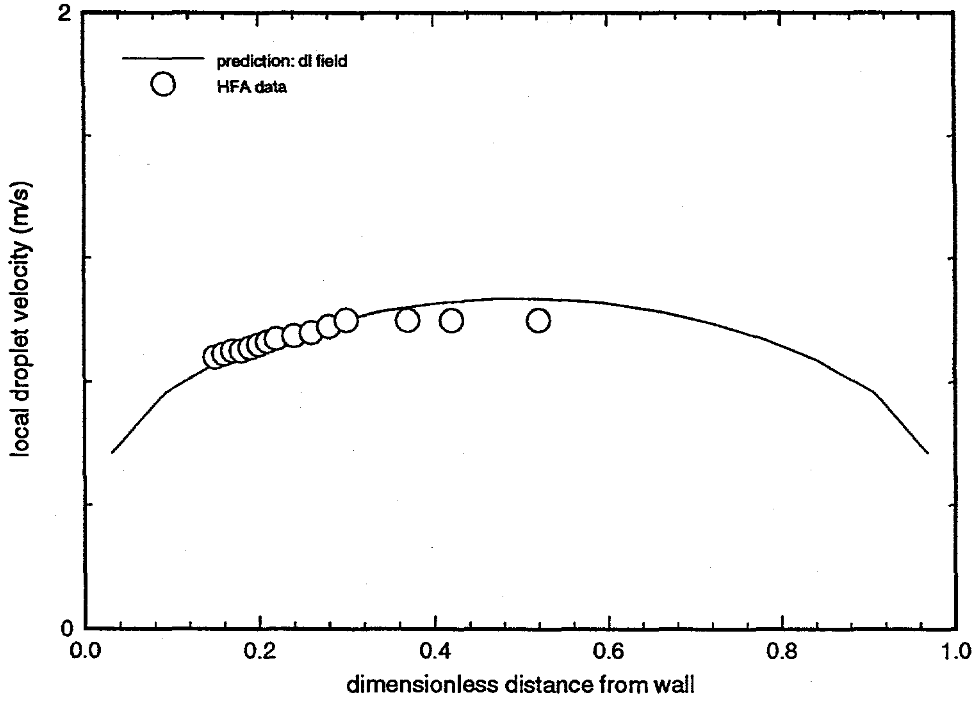

Figure 8: Comparison of Model Predictions with Experiments.

Case 5: P=2.4 MPa; w=106 kg/hr; $\overline{\alpha}$=0.90

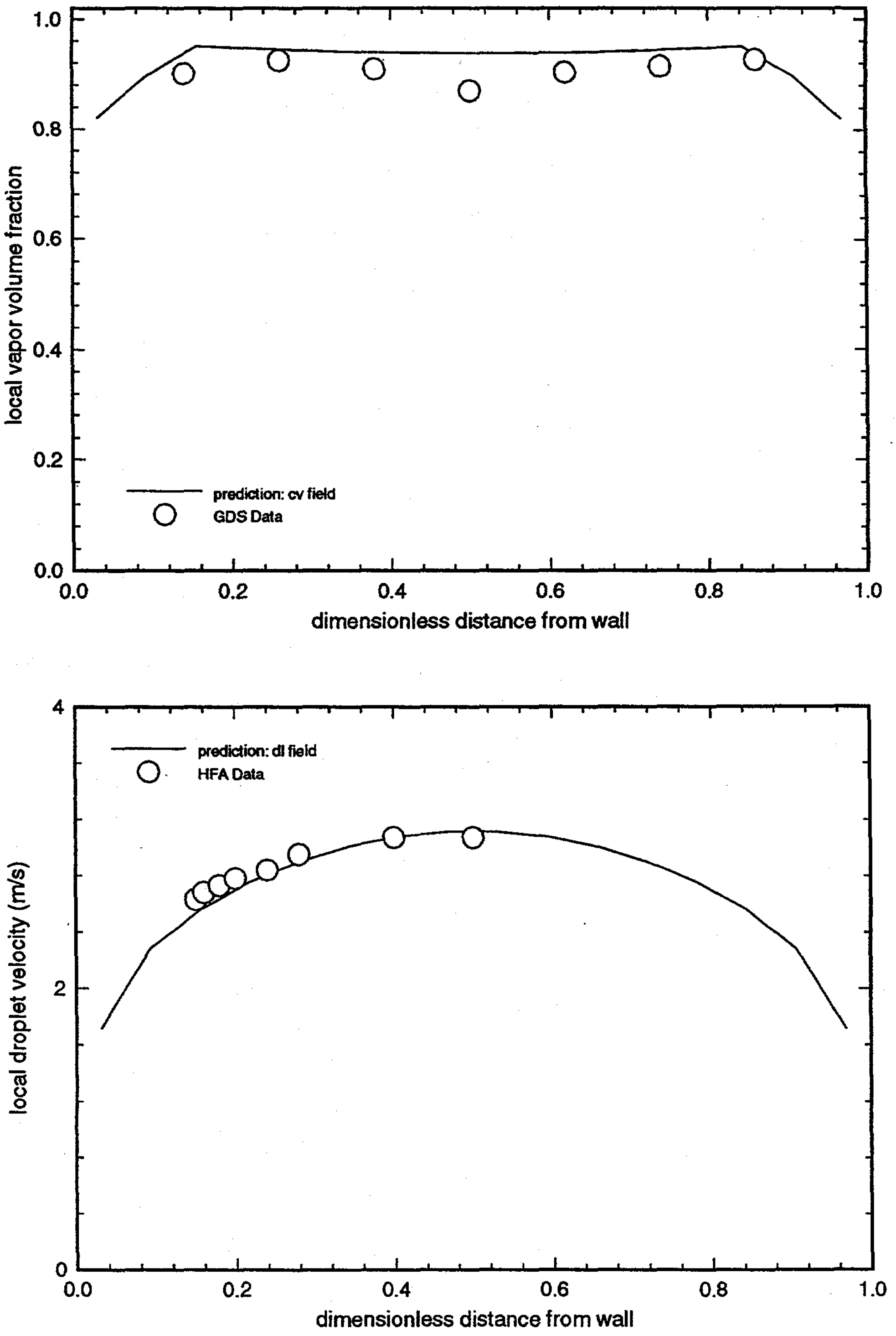

Figure 9: Comparison of Model Predictions with Experiments.

Case 6: P=2.4 MPa; w=266 kg/hr; $\bar{\alpha}$=0.92

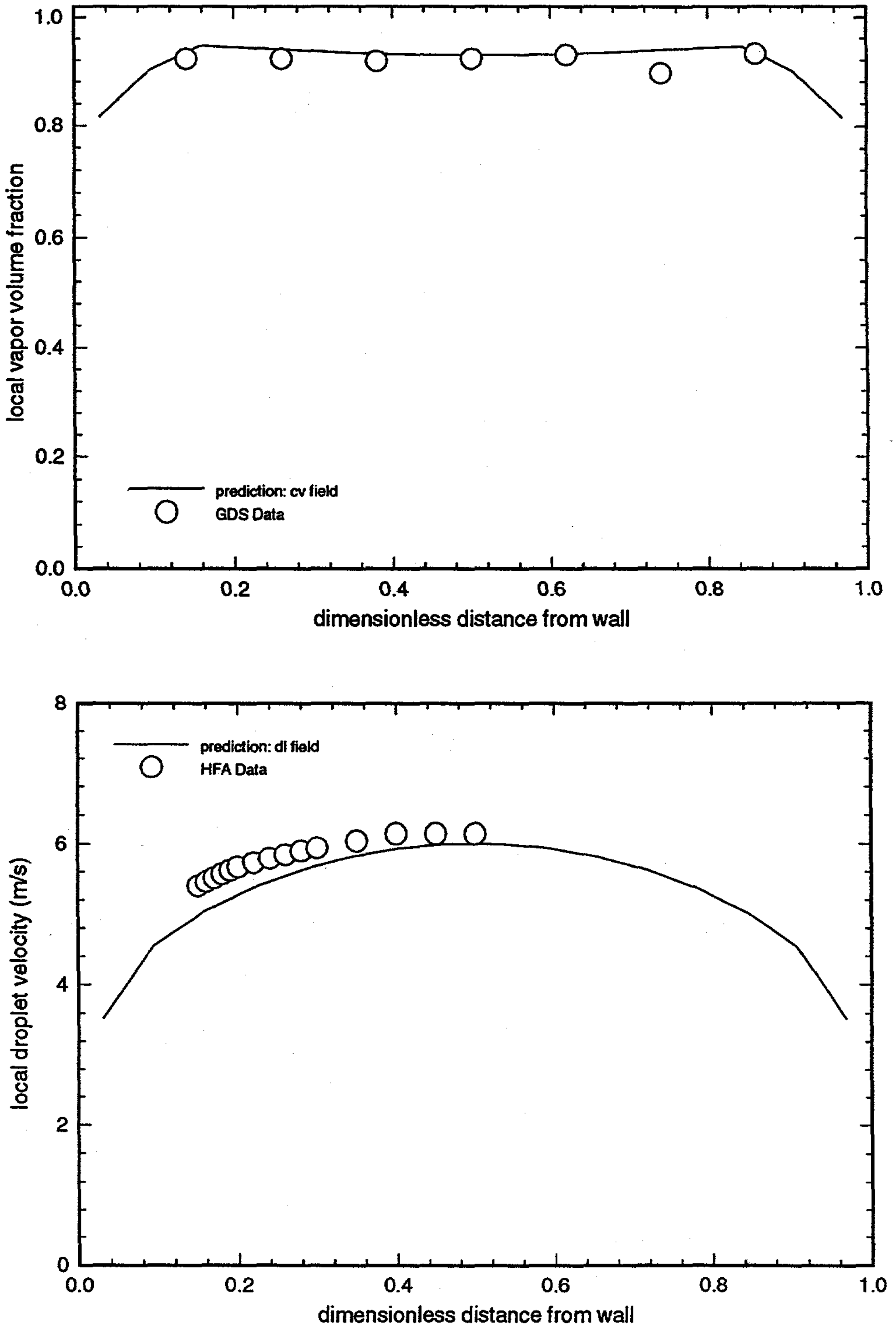

Figure 10: Comparison of Model Predictions with Experiments.

Case 7: P=2.4 MPa; w= 532 kg/hr; $\bar{\alpha}$=0.94

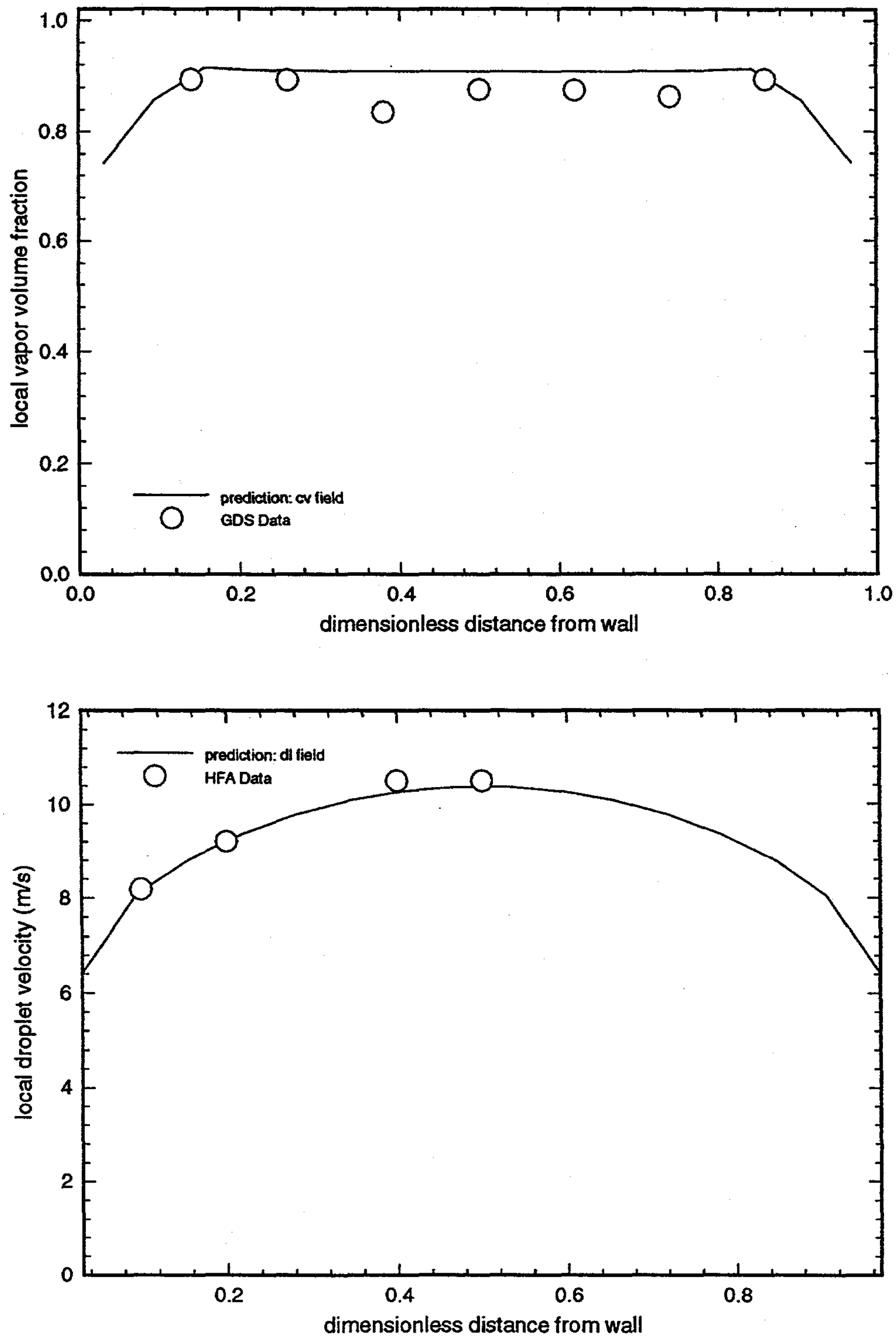

Figure 11: Comparison of Model Predictions with Experiments.

Case 8: P=2.4 MPa; w= 1064 kg/hr; $\overline{\alpha}$=0.90